Postglacial Relative Sea-Level Changes in the Gulf of Maine, USA: A Challenge for GIA Models

Audrey Baril

Thesis submitted to the University of Ottawa

in partial fulfillment of the requirements for the

Master's degree in Physics

Department of Physics
Faculty of Science
University of Ottawa

Abstract

Relative sea level (RSL) reconstructions from paleo records are often the most valuable data set in testing and constraining glacial isostatic adjustment (GIA) models. In some regions, the amplitude and rate of the reconstructed RSL changes are large making the data difficult to fit. Arguably, the reconstructed RSL curve from Maine, USA, is the classic example of such a data set with peak values at about 120 m dropping to a low stand of around -40 m within a few kyr. To our knowledge, no GIA model has captured these extreme variations and the record has been somewhat neglected by the GIA community. Here we critically assess and present a revised pre-10 ka RSL data base for this region and combine it with two recent Holocene compilations. To determine if a successful model fit can be found, output based on a parameter set of five ice models and 440, spherically symmetric, Maxwell Earth viscosity models was compared to the compiled data. Results show that none of the ice models produce a good fit for the large suite of 1D viscosity models considered. Specifically, the modelled timing and rate of RSL fall are generally too early and low, and the RSL low stand from the models is significantly higher than that observed. A model sensitivity analysis suggests that Earth models that can simulate time-dependent viscosity (e.g., those including transient and/or non-linear effects) are required to fit the Maine RSL data set.

Acknowledgements

I would like to thank my supervisor, Glenn Milne, for his great support and guidance throughout all the steps of this project. I learned a lot during those two years and acquired many skills that will be useful to me for the rest of my career thanks to you. I couldn't have achieved my goals without your much-appreciated help. I would also like to thank my collaborators, Ed Garrett, Joseph Kelley and Roland Gehrels for their help and advice during this research, as well as their significant contributions to the compilation and assessment of the new database used in this thesis.

To my parents, Yves and France, thank you for providing me with your love and support in all the ways you could. You encouraged me in every decision I made, and I will be forever grateful for this. Many thanks to my brothers, Francis and Sebastien, who provided great mental support by listening to me vent throughout this pandemic. And a special mention to my uncle Louis Amyotte, who left us, way too soon, at the beginning of this adventure. You're still in our hearts.

Table of contents

List of Acronyms

AMS: Accelerator Mass Spectrometry

ASL: Absolute sea level

GIA: Glacial Isostatic Adjustment

GMSL: Global Mean Sea Level

LGM: Last Glacial Maximum

LMV: Lower mantle viscosity

LT: Lithosphere thickness

MTL: Mean tide level

RSL: Relative sea level

SLIP: Sea level index point

UMV: Upper mantle viscosity

List of Figures

Chapter 1. Introduction

1.1. Motivation and Aims

In the past decades, global warming has become a source of concern due to its increasingly apparent social, economical, and ecological impacts [Ara Begum et al., 2022]. One major concern that motivates the research presented in this thesis is sea-level rise. As of 2022, the negative effects of rising sea levels are clearly apparent in many coastal regions. One of the most widely known ecological impact is the endangerment of various species, notably estuarian species. As saltmarshes become increasingly flooded, these environments release the accumulated sediment-associated carbon, nutrients, and pollutants, leading to habitat destruction [Haaf, 2022]. Effects on the ecosystem often lead to economical impacts: for example, in Vietnam, where drought and saline water intrusion damages the food production of the country for which the economical loss has been estimated at millions of dollars (US) every year [Park et al., 2022]. As for the social impact of sea-level rise, there are numerous examples of emerging conflicts, one of them being the need to sacrifice areas in Ho Chi Minh City in order to implement flood prevention measures to save other parts of the city [Hinkel et al., 2018].

To estimate and attempt to reduce the impacts associated with sea-level rise, accurate predictions are necessary. This requires an understanding of the dominant underlying processes that affect sea level in different regions. Some examples include: ocean density changes, ice-ocean mass exchange, sediment transfer and compaction and Earth deformation (section 1.2) due to ice-ocean mass exchange, commonly referred to as glacial isostatic adjustment (GIA) (section 1.3) [Church et al., 2013]. While these processes all impact RSL in some way, the extent of their impact varies depending on the time period and location of interest. For example, vertical land motion caused by tectonic activities is a good example of a process affecting RSL in specific regions of the globe [Klos et al., 2019] while greenhouse gas emissions due to anthropogenic activities is an example of a process occurring only in modern times. Different types of models are used to predict sea-level change related to different underlying processes. For example, Atmosphere-Ocean General Circulation Models compute the height of the sea surface as a reaction to natural and anthropogenic forcings (volcanic eruptions, solar irradiance, Greenhouse gas emissions). Geodynamic surface-loading models predict the RSL response to changes in surface ice-water mass redistribution as well as atmospheric pressure changes [Church et al., 2013]. GIA models are a type of geodynamic surface-loading models focussed on predicting RSL changes due to past ice-ocean mass exchange (section 1.3.1). In regions where past ice sheets recently existed, such as Canada, GIA is a significant contributor to contemporary sea-level change.

To determine the accuracy of models used to predict changes in sea level, observations of past changes are required to optimise model parameters and test the predictive accuracy of the model. In the case of GIA models, observations from the geological record are especially important as they constrain RSL since the last glacial maximum (LGM) around 25 ka [Milne et al., 2009]. They can capture large amplitude and complex signals from various locations (e.g., in the near field and far field of past major ice sheets) with far-field locations being used to infer past ice volume and near-field regions being used to better understand Earth rheology as well as the regional ice evolution (section 1.3.1).

This thesis will focus on testing a GIA model using a newly compiled and challenging paleo RSL data set from Maine, USA. This data set has been largely ignored by the modelling community due to the observed large amplitude and rapid RSL changes. We aim to assess the accuracy of the reconstruction and use the reliable data to optimise and test a GIA model. The results of this research will help our understanding of past and future sea-level changes in this region as well as our understanding of Earth rheology. As our region of study is located in the near field of a past ice sheet, knowledge about RSL changes and Earth rheology in this region can be related to locations near present ice sheets (Greenland and Antarctica) and improve predictions of future RSL changes associated with their deglaciation due to global warming.

1.2. Relative sea level

There are various ways of defining what sea level represents and how to measure it. The most precise way of observing sea-level in reference to the Earth's center of mass is by using satellite altimetry, which has been used since the beginning of the 1990's [Cazenave et al., 2017]. This technology measures sea-level by sending short pulses of microwave radiation of a specific power towards the surface of the Earth below the radar altimeter and analysing the reflected radiation to determine the height of the altimeter above the sea surface [Ablain et al., 2017]. This method computes the absolute sea-level (ASL) by comparing the height difference between the sea surface and the reference ellipsoid (Fig. 1.1). The reference ellipsoid is an ellipsoid of revolution that best matches the geoid surface, which is an equipotential surface to the gravitational field of the Earth that approximates the mean level of the sea surface over several years to decades.

Another way of defining sea level that is more pertinent to this study is termed relative sea level (RSL). RSL represents the thickness of a water column sitting over the Earth surface, notably the ocean floor in this case, at a given location. As the ocean floor elevation varies greatly all over the world, for example, the Mariana Trench with a depth of (10,984 ± 25) m at its lowest [Gardner et al., 2014] and the Indira with a depth of 1200m at its highest peak [Siddiquie et al., 1983], relative sea level is heavily dependent on location. In the past 100-150 years, tide gauges have been used to record relative sea-level at multiple locations on the globe. However, information from them is limited both in time and space as only a few gauges are older than 1880 [Gornitz, 1995]. To determine RSL changes for older times, information must be obtained from geological records. This information is referred to as proxy data, which are dated samples that provide information on sea level [Shennan, 1986] (see 1.4.1.).

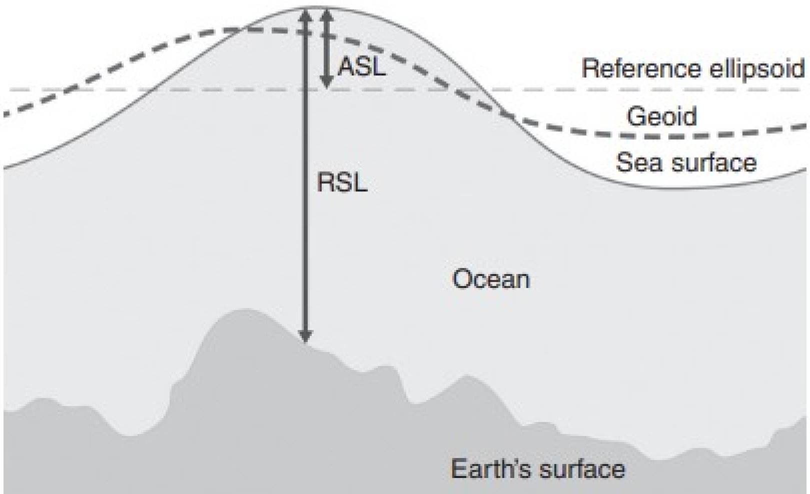

Figure 1.1 Schematic representation of different sea-level definitions: Relative sea level (RSL) and Absolute sea level (ASL). The geoid and reference ellipsoid are also indicated. [Figure 2.1 from Milne, 2015.]

As shown in Figure 1.2 below, many processes can affect relative sea level, meaning they influence the depth of the ocean at a given location. It is useful to divide these processes into two categories: the processes influencing the total volume of the oceans, thus causing a change in global mean sea level (GMSL), and the processes influencing the topography of the ocean floor and surface, thus producing spatial variations in RSL change. Some of these processes can also produce feedbacks on each other, be it negative or positive.

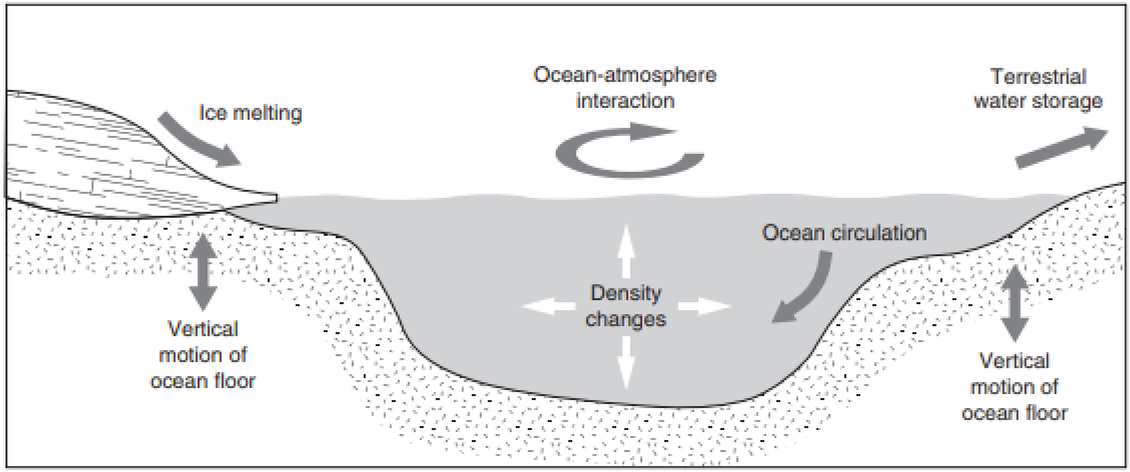

Figure 1.2 Schematic representation of some of the different processes affecting RSL, notably ice melting, density changes of the water and vertical land motion. [Figure 2.3 Milne, 2015]

An important source of RSL change on a variety of timescales is the melting of land ice which affects GMSL. Following the introduction of melt water to the ocean, water density will change due to the resulting changes in salinity and temperature as the meltwater is mixed into the water column. While these density (steric) changes impact sea-level on a regional scale, only the temperature of the water has a significant impact on GMSL [Church et al., 2013] and it is one of the main causes of present-day sea-level rise. During deglaciation, the influence of temperature change was largely counteracted by the influence of salinity coupled with the compression of the seawater [Gebbie, 2020].

Figure 1.2 shows that vertical motion of the ocean floor can affect RSL. Tectonic activity, such as near the Pacific coast of North America, is a good example of one of the causes of vertical ocean-floor motion due to the Cascadia subduction zone (e.g., Yousefi, 2021). Marine currents are also a source of topography changes. As they pass through a region, sediments can be transported in and out, affecting ocean depth. The addition of meltwater can change the geometry and strength of marine currents as well as accelerate sediment compaction on the ocean floor by increasing the water weight. Moreover, the increased pressure on the ocean floor by the additional water mass also triggers an isostatic response from the Earth. In fact, many processes can trigger an isostatic response as they disrupt the equilibrium between the lithosphere and the mantle (more specifically the asthenosphere). As the equilibrium is disrupted, the Earth's response is to go back to a state of equilibrium by changing shape.

1.3. Glacial Isostatic Adjustment

1.3.1. Overview

As the ice-water mass at the Earth's surface is redistributed by the growth or melting of ice sheets, the gravitational field, ocean volume, and the solid Earth are subjected to changes. As described above, these processes are commonly considered together, under the umbrella term GIA, which is classically aimed at studying these processes during the late Quaternary and especially since the LGM as the large deglaciation since then still impacts RSL changes to this day, especially in near-field locations. Figure 1.3 is a schematic representation of processes composing GIA for the case of a marine-based ice sheet.

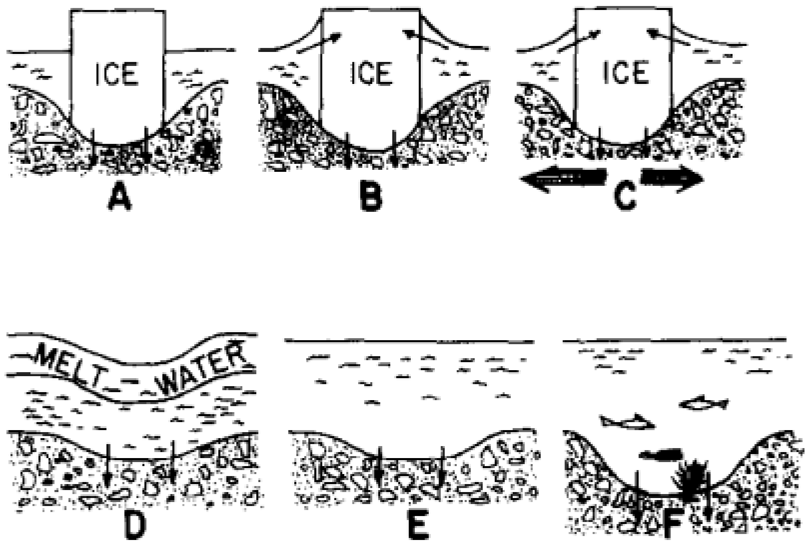

Figure 1.3 Schematic representation of GIA for a marine-based ice sheet. A) Deformation of the Earth by the ice sheet. B) Gravitational pull of the ice distorts the geoid. C) Deformation of the solid Earth distorts the geoid. D) Meltwater weight deforming the seafloor. E) Regional ocean load increased by depression left by ice sheet. F) Ocean floor deformation due to the increase in the ocean load. [Figure 1 from Clark et al, 1978]

Figure 1.3 (A) represents the deformation incurred from the presence of an ice sheet. The ground under the ice is pressed down under the weight of the ice sheet while the ground around it is uplifted. (B) shows the gravitational pull attracting more water towards the ice sheet, which will in turn deform the geoid; (C) also shows the gravity (geoid) change, but due to the solid Earth deformation associated with the ice and ocean loading. (D) shows the seafloor after the complete deglaciation of the ice sheet. An uplift is visible on the sea floor that was under the ice while the region around the ice, the peripheral bulge, has subsided. As the peripheral bulge collapses over time, the capacity of the ocean basin increases too. This process is called ocean syphoning (Mitrovica and Milne, 2002). Even though the land is released from the ice sheet's weight, the weight of the melt water still deforms the Earth. As water fills the depression on the ocean floor, the ocean load increases (E) which is an important component of the sea-floor deformation (F). As the ocean loading increases due to the GMSL rise, an important and geographically widespread characteristic called continental levering takes place as the seabed is pushed downward resulting in the landward part of the coast moving upward (Clark et al., 1978).

When considering RSL changes related to GIA, three general temporal patterns can be identified depending on the proximity of the studied area to the location of past ice sheets. Locations in the near-field of the ice sheet, which were previously ice covered, tend to experience a significant drop in sea level as the ocean floor which was sunken because of the ice sheet's mass emerges subsequent to deglaciation. Locations in the forebulge of the ice sheet, beyond the margin of the ice sheet at the LGM, show a different pattern as the motion of the sea floor is characterised by subsidence throughout deglaciation which results in a rise in sea level. It is important to note that locations on the margin of an ice sheet, which start as a near field region and become a peripheral region later on, can exhibit both patterns with a transition from emergence to subsidence as the forebulge migrates inwards to the centre of ice loading. At locations in the far-field of the ice sheets, RSL changes are dominated by the GMSL signal (meltwater plus syphoning) with ocean loading also playing a significant role. This is reflected by a rise in sea level during the main phase of ice melting (~18000 to ~6000 years ago).

As GIA-related RSL changes are strongly dependent on the ice extent history and Earth deformation, the two primary inputs to models of this process are a reconstruction of past ice changes and a model that defines the Earth rheology and density structure (section 1.3.2.). A Maxwell model of Earth rheology has generally been able to fit GIA data well in various areas and so it has been most commonly applied in GIA modelling studies. Thus, all stresses have been assumed to have a linear relation to strain rate. In this research, a spherically symmetric GIA model is used in which material properties vary only with depth. As such, no lateral variations of the mantle viscosity have been taken into consideration. However, it is known that the real Earth can exhibit non-linear deformation and has lateral variation in its viscosity structure. More elaborate models have been developed that take these aspects into consideration (e.g., Whitehouse, 2018) but they are not considered in this thesis. While the ice-loading response is calculated directly from the ice model, the ocean-loading response and changes in Earth rotation are obtained by solving the sea level equation (section 1.3.3.).

1.3.2. Modelling Earth Deformation

As noted above, in GIA studies the Earth's rheology is often represented as a Maxwell material, meaning that it possesses both the properties of an elastic and viscous material. The reason for this assumption lies in the fact that GIA considers timescales in which both elastic and viscous properties of the Earth are significant in the deformational response, and thus affect RSL.

As a simplification, only the off-diagonal elements (shear stress and shear strain) will be considered in this section. In an elastic rheology, the relation between stress (τ) and strain (e) is represented in a linear way:

$$\mathrm{e}(t) = \frac{\tau(t)}{2\mu} \tag{1.1}$$

Where μ is the elastic shear modulus of the material.

For linear viscous materials, the relation between stress and strain is represented by:

$$\frac{d\mathrm{e}(t)}{dt} = \frac{\tau(t)}{2\nu} \tag{1.2}$$

Where ν is the viscosity of the material.

In a Maxwell material, the strains can be added together such that the total strain can be written:

$$e_{Total}(t) = \frac{\tau(t)}{\mu} + \int_{t_0}^{t} \frac{\tau(t)}{\nu} \tag{1.3}$$

To compute the solid Earth's response to an impulse load disrupting its equilibrium state, momentum conservation dictates that the response follows the linearized momentum equation:

$$\vec{\nabla}\tilde{T}_1 + \vec{\nabla}(\vec{u}\vec{\nabla})\tilde{T}_0 - \rho_1\vec{\nabla}\phi_0 - \rho_0\vec{\nabla}\phi_1 = 0 \tag{1.4}$$

Where $\tilde{T}_0$, ϕ_0 and ρ_0 are, respectively, the stress tensor, the gravitational field and the density as a function of radius at equilibrium. $\tilde{T}_1$, ϕ_1 and ρ_1 indicate the perturbation to each of those fields to an impulse load. $\vec{u}$ is the load-induced vector displacement field.

As matter is conserved in this system, the perturbated density and the density at equilibrium must be related by the continuity equation:

$$\rho_1 = -(\vec{\nabla}\vec{u})\rho_0 \tag{1.5}$$

Changes in the mass distribution, which also affect the potential field, are represented by Poisson's equation:

$$\nabla^2\phi_1 = -4\pi G(\vec{\nabla}\vec{u})\rho_0 \tag{1.6}$$

In which G is the gravitational constant.

To determine the parameters ϕ_1 and $\vec{u}$, other parameters such as $\tilde{T}_1$ and ρ_1 should be expressed using ϕ_1 and $\vec{u}$. In the case of ρ_1, equation 1.5 can simply be substituted into equation 1.4. For $\tilde{T}_1$, the constitutive equation of a Maxwell viscoelastic rheology is applied:

$$\tau_{ij} + \frac{\mu}{\nu}\left(\tau_{ij} - \frac{1}{3}\tau_{rr}\delta_{ij}\right) = 2\mu\dot{e}_{ij} + \lambda\dot{e}_{rr}\delta_{ij} \tag{1.7}$$

With τ_{ij} and τ_{rr} being, respectively, the ij^th component and the summation (i.e., $\tau_{rr} = \tau_{11} + \tau_{22} + \tau_{33}$) of components of $\tilde{T}_1$. μ and λ are the elastic Lamé parameters, ν is the viscosity and δ_{ij} is the Kroneker delta (1 if i=j, 0 otherwise).

From the correspondence principle, the Laplace transform of equation 1.7 gives:

$$\check{\tau}_{ij} = \lambda(s)\check{e}_{rr}\delta_{ij} + 2\mu(s)\check{e}_{ij} \tag{1.8}$$

In which the inverted circumflex shows implicit dependence to Laplace transform variable s. $\lambda(s)$ and $\mu(s)$ are respectively:

$$\lambda(s) = \lambda + \frac{\frac{2}{3}\mu\left(\frac{\mu}{\nu}\right)}{s + \frac{\mu}{\nu}} \quad \text{and} \quad \mu(s) = \frac{\mu s}{s + \frac{\mu}{\nu}} \tag{1.9}$$

Then equation 1.4 combined with 1.5 can be converted to a Laplace transform and combined with equation 1.8 to solve the momentum equation for ϕ_1 and $\vec{u}$. The Poisson equation (1.6) is also simultaneously solved as a Laplace transform in order for the solutions to be gravitationally self-consistent. The solutions can be expressed as an infinite series of Legendre polynomials:

$$u(a,\gamma,t) = \sum_{\ell=0}^{\infty} u_\ell(a,t)P_\ell\big(cos(\gamma)\big) \tag{1.10}$$

$$v(a,\gamma,t) = \sum_{\ell=0}^{\infty} v_\ell(a,t)\frac{\partial}{\partial\gamma}P_\ell\big(cos(\gamma)\big) \tag{1.11}$$

$$\phi_1(a,\gamma,t) = \sum_{\ell=0}^{\infty} \phi_{1,\ell}(a,t) P_\ell\big(cos(\gamma)\big) \tag{1.12}$$

In which $u(a,\gamma,t)$ and $v(a,\gamma,t)$ are the radial and tangential components of $\vec{u}$ at the Earth's undeformed surface (where r = a). $\phi_1(a,\gamma,t)$ is the pertubation of the surface's geopotential. $P_\ell\big(cos(\gamma)\big)$ are Legendre polynomials of the cosinus of γ, the great circle angle between the impulse load point and the observation point. Their coefficients are:

$$u_\ell(a,t) = u_\ell^E \delta(t) + \sum_{k=1}^{K} \delta u_{\ell,k}^{NE} exp\big(-s_k^\ell t\big) \tag{1.13}$$

$$v_\ell(a,t) = v_\ell^E \delta(t) + \sum_{k=1}^{K} \delta v_{\ell,k}^{NE} exp\big(-s_k^\ell t\big) \tag{1.14}$$

$$\phi_{1,\ell}(a,t) = \phi_{1,\ell}^E \delta(t) + \sum_{k=1}^{K} \delta \phi_{1,\ell,k}^{NE} exp\big(-s_k^\ell t\big) \tag{1.15}$$

The components u_ℓ^E, v_ℓ^E and $\phi_{1,\ell}^E$ which are associated to the dirac Delta function $\delta(t)$ represent the elastic response. $\delta u_{\ell,k}^{NE}$, $\delta v_{\ell,k}^{NE}$ and $\delta \phi_{1,\ell,k}^{NE}$, which are related to the non-elastic response, are associated with an exponential function characterized by inverse decay time s_k^ℓ. As it is customary to use dimensionless numbers, those coefficients are then transformed into viscoelastic Love numbers:

$$\begin{pmatrix} h_\ell^L(t) \\ l_\ell^L(t) \\ k_\ell^L(t) \end{pmatrix} = \frac{g}{\phi_{2,\ell}(\mathrm{a})} \begin{pmatrix} u_\ell(a,t) \\ v_\ell(a,t) \\ -\dfrac{\phi_{3,\ell}(a,t)}{g} \end{pmatrix} \tag{1.16}$$

The Love numbers $h_\ell^L(t)$ and $l_\ell^L(t)$ are, respectively, the radial and tangential displacement fields and the Love number $k_\ell^L(t)$ is the perturbation to the gravity field. The superscript L indicates their relation to the surface mass loading. The constant g is the Earth's gravitational acceleration and $\phi_{2,\ell}(a)$ is the component from the Legendre expansion of the perturbation to the surface gravity field caused by the direct attraction of the surface load. The Love numbers can be expressed with an implicit time dependence as such:

$$h_\ell^L(t) = h_\ell^{L,E}\delta(t) + \sum_{k=1}^{K} r_k^{\ell,L} exp\left(-s_k^\ell t\right) \tag{1.17}$$

$$l_\ell^L(t) = l_\ell^{L,E}\delta(t) + \sum_{k=1}^{K} \hat{r}_k^{\ell,L} exp\left(-s_k^\ell t\right) \tag{1.18}$$

$$k_\ell^L(t) = k_\ell^{L,E}\delta(t) + \sum_{k=1}^{K} \check{r}_k^{\ell,L} exp\left(-s_k^\ell t\right) \tag{1.19}$$

These Love numbers allow us to define Green's functions for the load-induced radial displacement of the solid surface $\Gamma^L(\gamma, t)$ as well as the load-induced perturbation to the Earth's gravitational potential at the undeformed surface $\Upsilon^L(\gamma, t)$:

$$\Gamma^L(\gamma, t) = \frac{a}{M_e}\sum_{t=0}^{\infty} h_\ell^L P_\ell\left(cos(\gamma)\right) \tag{1.20}$$

$$\Upsilon^L(\gamma, t) = \frac{ag}{M_e}\sum_{t=0}^{\infty} (\delta(t) + k_\ell^L) P_\ell\left(cos(\gamma)\right) \tag{1.21}$$

The radial displacement and perturbation to gravity for a more general surface load is computed by convolving these Green's functions in space and time with the load history.

1.3.3. Sea Level Equation

As described above, the sea-level change is a component of the ocean load which governs the GIA-driven RSL response. Thus, solving for the ocean load (and thus RSL) is non-trivial. Farrell and Clark [1976] included the relevant processes in an equation, known as the sea-level equation, the solution of which gives the ocean load (and RSL change) due to GIA. More recent work has extended the original equation to include time dependent shorelines [Mitrovica and Milne, 2003; Kendall et al., 2005] and Earth rotation [Milne and Mitrovica, 1998; Mitrovica et al., 2005] to refine the equation in order to better predict RSL. A general expression of the sea-level equation as introduced by Farrell and Clark [1976] is:

$$S(\theta, \psi, t) = C(\theta, \psi)[\mathrm{G}^L(\theta, \psi, t) - \mathrm{R}^L(\theta, \psi, t)] \tag{1.22}$$

$\mathrm{S}(\theta, \psi, \mathrm{t})$ defines the change in sea level at a given latitude θ, longitude ψ and time t (relative to a defined reference time). $\mathrm{G}^L(\theta, \psi, t)$ and $\mathrm{R}^L(\theta, \psi, t)$ are respectively the load-induced deformation of the geoid and seafloor at given coordinates and time. $C(\theta, \psi)$ represents the Ocean function which varies according to the coordinates and time such that:

$$C(\theta, \psi) = \begin{cases} 0 & \mathit{On\ land} \\ 1 & \mathit{In\ the\ ocean} \end{cases} \tag{1.23}$$

It is important to note that the ocean function will vary with time due to shoreline migrations. This is taken into account by the model applied in Chapter 2, however for simplicity, only the time independent ocean function case will be described in this section.

The load-induced deformations $\mathrm{R}^L(\theta, \psi, t)$ and $\mathrm{G}^L(\theta, \psi, t)$ can be defined as:

$$\mathrm{R}^L(\theta, \psi, t) = \int_{-\infty}^{t} \iint_{\Omega} a^2 L(\theta', \psi', t')\Gamma^L(\gamma, t - t')d\Omega' dt' \tag{1.24}$$

$$\mathrm{G}^L(\theta,\psi,t)=\frac{\Phi^L(\theta,\psi,t)}{g}+G^L(t)=\int_{-\infty}^{t}\iint_{\Omega}\frac{a^2}{g}L(\theta',\psi',t')\Upsilon^L(\gamma,t-t')d\Omega'dt'+G^L(t)\quad(1.25)$$

Where Ω is the spatial integration unit over a sphere, $\Phi^L(\theta,\psi,t)$ is the load induced perturbation to the gravity field, $L(\theta',\psi',t')$ is the surface mass load and $G^L(t)$ is the height shift of the geoid incurred by the conservation of the surface mass load while perturbations to the geoid occur. The surface mass load can be defined:

$$L(\theta,\psi,t)=\rho_I I(\theta,\psi,t)+\rho_w S(\theta,\psi,t)\qquad(1.26)$$

With $I(\theta,\psi,t)$ and $S(\theta,\psi,t)$ respectively being the thickness of the ice and the thickness of the water column at given time and coordinates and ρ_I and ρ_w being their respective densities.

Therefore, the sea level equation can be written as:

$$S(\theta,\psi,t)=C(\theta,\psi)\left[\int_{-\infty}^{t}\iint_{\Omega}a^2\rho_I I(\theta',\psi',t')\left\{\frac{\Upsilon^L(\gamma,t-t')}{g}-\Gamma^L(\gamma,t-t')\right\}d\Omega'dt'+\right.$$
$$\left.\int_{-\infty}^{t}\iint_{\Omega}a^2\rho_w S(\theta,\psi,t)\left\{\frac{\Upsilon^L(\gamma,t-t')}{g}-\Gamma^L(\gamma,t-t')\right\}d\Omega'dt'+\mathrm{G}^L(\mathrm{t})\right]\qquad(1.27)$$

As the unknown component $S(\theta,\psi,t)$ is found on both sides of the sea level equation, equation 1.27 is an integral equation. Different approaches have been applied to solve this equation but the most commonly applied is the pseudo-spectral method [Mitrovica and Peltier, 1991] which solves the sea level equation by using an iterative technique. This was the method applied in the research presented in Chapter 2 of this thesis.

1.4. Sea-level reconstruction using proxy records

1.4.1. General methods of RSL reconstruction

There are three categories of geological sea-level indicators: geomorphological, lithological, and biological. Geomorphological evidence refers to the morphological features formed only in coastal areas. For example, coastal landforms which have emerged or have been submerged (rock platforms, beaches, deltas, coral reefs, etc.) can indicate past relative sea levels [Lowe & Walker, 2014]. Lithological evidence refers to the observations from sediments. As sediments are different depending on the type of climate and environment (glaciogenic deposits, pluvial lake sediments, wind blown sediments, etc.), their observation coupled with geomorphological evidence can provide a better understanding of past RSL elevations. Biological evidence refers to remains of plants and animals called macro or micro fossils [Ruddiman, 2008]. In sea-level reconstruction, the most common approach is to date biological evidence fulfilling specific conditions to be used as paleo sea-level constraint. This category of evidence can also be compared to geomorphological and lithological evidence to ensure the location of the sample is consistent with its natural habitat. In fact, to be used to reconstruct sea-level, a given sample must be found *in-situ* (i.e., within its habitat) in the location where one wishes to reconstruct sea level and be dated (usually with radiocarbon dating (section 1.4.2)). Also, information must be available relating to the elevation of habitat compared to a given height within the tidal range such that past mean sea-level can be estimated (the so-called "indicative meaning") [Khan et al., 2019]. A few more details are required to be able to use the samples found on site, but they pertain mostly to the collection method, the laboratory processing, the condition of the sample, etc., which are outside the scope of this thesis.

Geological samples or markers used in reconstructing past sea-level give a broad range of precision. sea-level index points (SLIPs) are a two-way constraint which indicates a specific sea-level range (maximum and minimum) where the sea level stood in the past [Milne, 2015]. Marine limiting points are a one-way constraint indicating that sea level existed above the height associated with that data point. Terrestrial limiting points are also a one-way constraint but are the inverse of a Marine limiting point in that they indicate an altitude that sea level must have been below. Those are the three kinds of RSL constraints obtained from geological proxies. While SLIPs are generally the most useful sea-level data points because of their precision, limiting data is important to consider when validating the accuracy of SLIPs or in locations and time periods with few SLIPs.

The type of sea-level constraint a biological sample provides (i.e., SLIP vs limiting) is determined by the species of the specimen. A species habitat will vary in accordance to relative sea level. For example, SLIPs can come from species that live in shallow water habitats such as saltmarshes. The indicative meaning of different species is determined by studying their distribution relative to mean sea level in the present day and this information is assumed to remain valid for making paleo reconstruction based on fossils of the same (or related) species. Geomorphological features such as beach and river delta deposits can also be used to produce SLIPs (e.g., Thompson et al., 1989). Terrestrial limiting data tends to come from specimens such as tree stumps and freshwater lakes while marine limiting data tends to come from marine and glacio-marine deposits and the species contained within these (e.g., Vacchi et al. 2018). To be accepted as a valid data point, a sample must be examined thoroughly in order to determine if it has been transported since its death. A sample that is badly conserved (e.g., fragmented) or in an unconventional orientation relative to sedimentary bedding planes could indicate that it is not *in-situ*. Samples found with other materials that could affect their ^{14}C levels (e.g., plant root penetration, limestone, etc.) are also avoided.

Since Accelerator Mass Spectrometry (AMS) technology became available, around 1977 [Bennet et al., 1977; Nelson et al., 1977; Purser et al., 1977], the age determination of sea-level data has been obtained using this method as it is a very precise and quick process that requires only small samples [Jull, 2013]. Prior to 1977, samples were dated using other technologies such as the screen wall counter [Anderson et al., 1951] for solid-source counting (which had low efficiency and required large samples), photomultiplier tubes for liquid scintillation counting (which was efficient with small samples but time consuming), and gas counters for gas proportional counting, which was also efficient [Cook & van der Plicht, 2007]. While solid-source counting did not give out precise enough results and was ultimately rejected as a dating method, liquid scintillation counting, and gas proportional counting gave precise results and were used prior to the availability of AMS methods. As some of the data used in this thesis were published in the 1960s, these older dating techniques may have been used.

1.4.2. Radiocarbon dating of paleo sea-level indicators

It is well known that radioactive decay is an efficient dating method in many scientific fields. This principle stems from measuring the quantity of a given isotope in a specimen using AMS and computing its age based on this information and the half-life of the isotope. The type of isotope used for dating depends on what geological period one wishes to reconstruct an age. As various isotopes have different values of half-life, using an isotope with a much smaller half-life than the period of interest would be inadequate. A good example of suitable isotopes for dating a given time period would be using Rubidium 87, Uranium 238 and Uranium 235 to date samples from time periods over 100 Myr as they have a longer half-life than isotopes like Carbon 14. Since the half-life of the ^{14}C isotope is known to be around 5.78kyrs, it is commonly used for dating samples younger than 50 ka old samples [Ruddiman, 2008]. As such, radiocarbon dating is a very effective way to date paleo sea-level data since the last glacial maximum (~21 ka). Another reason why ^{14}C is preferred over other isotopes, is that the beta particles emitted during decay have very low energy, meaning that they cannot penetrate a sample from the exterior, which minimizes contamination [Cook & van der Plicht, 2007]. Any interference from an external source is bound to produce a larger uncertainty in the data, which needs to be avoided when reconstructing past events such as sea level changes.

One limitation of the standard calculation for dating isotopes is that the time reflected by the number of ^{14}C atoms is heavily dependant on the initial amount at the time when the item no longer incorporates ^{14}C from the atmospheric or marine environment. Indeed, since carbon 14 is a cosmogenic isotope, the concentration of ^{14}C found in the biosphere greatly depends on the number of cosmic rays penetrating the atmosphere. As one can expect, the rate of production of ^{14}C has varied in the past due to a multitude of processes (e.g., the strength of the Earth's magnetic field, variations in solar activity, variation of cosmic ray flux) [O'brien, 1979; Reimer and Reimer, 2007; Quarta et al, 2021]. The resulting variations of ^{14}C concentration can in turn affect the accuracy of radiocarbon dating. For example, a larger initial concentration of ^{14}C at the time of death could make a sample appear younger while a small initial concentration would make the sample appear older. Thus, calibration curves have been constructed using data from tree rings, U/T dated corals and any other absolutely dated proxy records [Quarta et al., 2021; Stuiver et al., 2022] to accurately depict the concentration of ^{14}C throughout time in both the atmosphere and the hydrosphere to help with sea-level reconstruction. Figure 1.5 shows the latest calibration curves which are input to software used to calibrate the radiocarbon-14 ages obtained via AMS methods. $\Delta^{14}C$ represents the difference between the ^{14}C concentration at a given time and the reference value assumed in 1950 (in per mil and corrected for radiocarbon decay) [Stuiver & Polach, 1977].

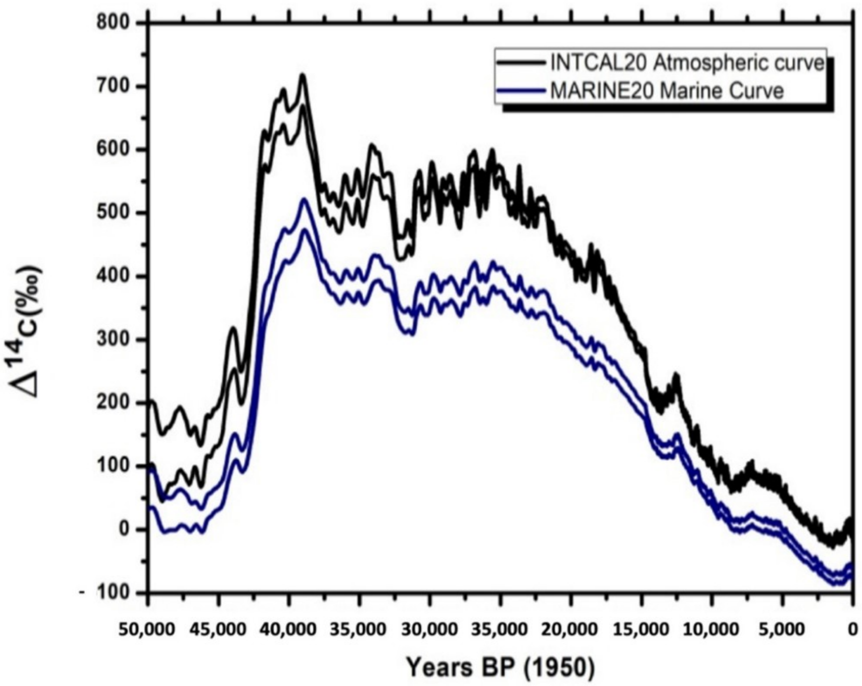

Figure 1.4 Latest calibration curves for atmospheric (INTCAL20) and oceanic (MARINE20) **Δ**^{14}C for the past 50 000 years. [Figure 3 from Quarta et al., 2021]

From Figure 1.4, it is evident that the MARINE20 calibration curve shows lower ^{14}C concentrations that fluctuate less compared to the INTCAL20 curve since the atmospheric carbon reservoir is directly affected by cosmic rays while it takes other processes to introduce carbon to the marine reservoir. Modern day data confirms that atmospheric carbon 14 levels are significantly higher than marine carbon-14 levels, making samples formed in surface ocean water appear, on average, 400 years older than a sample formed at the same time in the atmosphere [Reimer and Reimer, 2007]. This observation, referred to as the marine reservoir age, is used to construct the curves for a better calibration of the data. If a marine specimen was to be calibrated using the atmospheric curve, the dating would make the sample appear older than its true age as the initial concentration of ^{14}C would be lower than indicated, hence the need for a separate curve to calibrate marine geological proxies. Figure 1.4 also shows that present carbon-14 levels tend to be lower than those from the past 50 000 years, thus reflecting the importance of the calibration process in radiocarbon dating.

One major limitation in generating calibration curves is that the very precise method of using tree rings as an indicator of atmospheric carbon levels (e.g., Becker and Kromer, 1993) only provides information for roughly 14 000 calibrated years in the past. Earlier data used to construct a calibration curve before this time tend to have a larger uncertainty, which will influence the accuracy of the curves. Another issue is the poorly constrained marine reservoir age prior to the Holocene (11 ka to present) which varies depending on the region the data came from. As such, 3-D ocean models have been used to determine marine reservoir ages at specific locations (e.g., Butzin et al., 2017).

Chapter 2. Postglacial Relative Sea-Level Changes in the Gulf of Maine, USA: Database Compilation, Assessment and Modelling.

2.1. Introduction

As the present ice sheets continue to melt with ongoing global warming, understanding, and quantifying the associated sea-level changes becomes increasingly important. One route towards this goal involves considering records of ice sheet and sea-level changes since the last glacial maximum to better understand the deglaciation process and its sea-level response. In addition to seeking a better understanding of the underlying processes, the influence of the most recent deglaciation continues to impact global changes in sea level through the process of glacial isostatic adjustment: the response of the solid Earth to changes in land ice (e.g., Peltier, 1999; Riva et al., 2009), which is particularly strong in locations of past major ice sheets such as North America and Eurasia (e.g., Slangen et al., 2012). GIA models, which solve the sea-level equation [Farrell and Clark, 1976] using information on ice history and Earth rheology [Whitehouse, 2018], have been tested and refined using sea level reconstructions from geological records (e.g., Peltier and Andrews, 1976; Lambeck et al., 1998; Simpson et al., 2009; Tarasov et al., 2012; Roy and Peltier, 2015). These calibrated models play an important role in understanding past and projecting future sea-level changes (e.g., Love et al., 2016).

Data from various regions can be used to test GIA models and constrain parameters. For example, as the influence of GIA is less significant in far-field regions, observations from these regions are typically used to constrain changes in global ice volume [Milne, 2015]. On the other hand, regions in the near-field of past ice sheets, where the GIA signal dominates, the observed sea-level response is used to infer information on the regional ice history and Earth rheology [Milne, 2015]. These records are typically more difficult to fit given the large spatial variations and sensitivity to parameters relating to both the forcing (ice history) and response (solid Earth). This is particularly true for ice-marginal records where the RSL response is highly non-monotonic due the local isostatic response being of similar amplitude to the global barystatic signal [Khan et al., 2015], which is related to the addition or removal of water mass to the ocean [Gregory et al., 2019]. These records are typically characterised by an early and rapid RSL fall followed by a lowstand and rise through the Holocene (e.g., James et al., 2005; Kelley et al., 2010) and thus present a challenging target for GIA models [James et al., 2009; Yousefi et al., 2018]. The more rigorous test provided by these data is important given emerging evidence for an isostatic response that departs from the Maxwell rheology commonly assumed in GIA models (e.g., Lau et al., 2021) and the importance of the isostatic response for simulating ice margin evolution (e.g., Gomez et al., 2012; Whitehouse, 2018; Han et al., 2021).

In this study, we compile, assess and model a RSL database for the Gulf of Maine, USA, where relative sea level displays a complex and large magnitude signal (e.g., Kelley et al., 2010). RSL reconstructions from this region are compatible with regional deglaciation around 15 ka preceding a large RSL fall which ended in a lowstand near 12 ka followed by a RSL rise that includes a period of relatively low rates of rise (termed a "slowstand") from 10.5 ka to 7.5 ka [Kelley et al., 2010]. From the data gathered in Kelley et al. [2010], the RSL fall is estimated to be around 160 m from 15 ka to 12 ka averaging a RSL change rate of -53.3 m/kyr. Such a rapid and large signal represents a challenge for GIA models.

Previous GIA modelling studies have considered RSL data from Maine (e.g., Roy and Peltier, 2015; Engelhart et al., 2011). However, they focussed on Holocene data only which can, in general, be fit well by GIA models. However, the pre-Holocene data which capture the rapid RSL fall and lowstand have largely been ignored by the modelling community. Our primary aims are: (1) to compile and assess a pre-Holocene database for this region using agreed community protocols [Khan et al., 2019] and (2) seek to fit this challenging dataset using a GIA model.

2.2. Methods

2.2.1 Data compilation and assessment

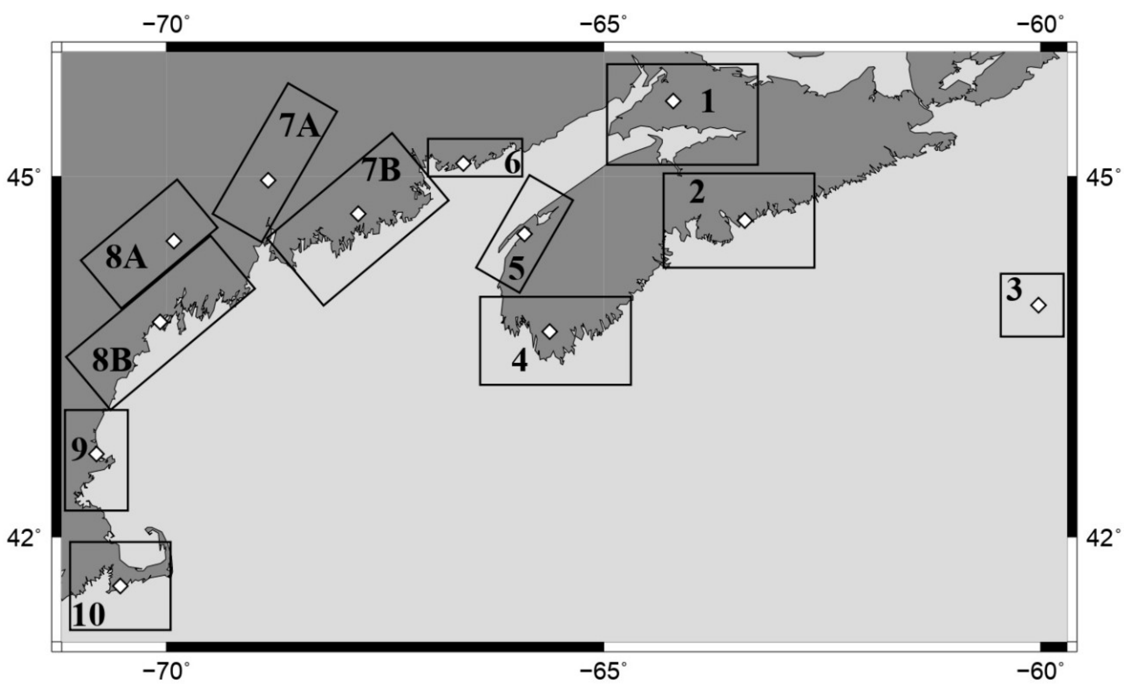

Figure 2.1 Map showing data subregions (black squares) and the mean data site location within each (diamonds) that is used to generate model RSL curves for each subregion.

The region of study ranges from Nova Scotia, Canada, in the north to Massachusetts, USA, in the south (Fig. 2.1). For this region, we compile a database of sea-level indicators from the literature, focussing primarily on the period before 10 ka that is not extensively covered by the two existing databases [Engelhart and Horton, 2012; Vacchi et al., 2018]. We follow the database format set out by Hijma et al. [2015] and widely implemented in the compilation of Holocene sea-level databases from around the world [Khan et al., 2019]. We classify each sea-level indicator as either a sea-level index point, which provides the elevation of RSL at a specific location and point in time, or a limiting point, which provides a minimum or maximum constraint on RSL.

For each SLIP, we assess the *indicative meaning*, the relationship between the indicator and contemporaneous tidal levels [Van de Plassche, 1986; Shennan, 2015]. The indicative meaning, incorporating a midpoint, or *reference water level*, and uncertainty, or *indicative range*, varies between different sea-level indicators. The majority of SLIPs in our database stem from subaerially exposed glaciomarine delta topset-foreset contacts [Thompson et al., 1989]. Sequence stratigraphic studies commonly ascribe a reference water level of approximately mean sea level [Chappel, 1974; Gobo et al., 2015], although few studies have explicitly validated this with modern observations. We tentatively assign an indicative meaning of 3 m below mean tide level (MTL) to MTL, following recommendations from Fernlund [1988] and Berglund [1992]. We do not derive SLIPs from submerged palaeodeltas as the topset-foreset contact cannot typically be confidently discerned in seismic reflection datasets and may be eroded by subsequent transgressions [Barnhardt et al., 1995; 1997]. Nevertheless, we use these geomorphic features and the elevation of fluvial incision [Knebel and Scanlon, 1985] to corroborate quantitative reconstructions of the depth of the lowstand obtained from other data sources. Fine-grained estuarine facies containing well-preserved intertidal or shallow subtidal bivalves provide a small number of SLIPs; however, several of these are of critical importance in defining the depth of the lowstand [Lee, 2006]. For these samples, we assign indicative meanings with reference to literature on the depth distributions of the particular species of bivalves encountered, as discussed in section 3.

The majority of marine limiting points in our database relate to the glaciomarine sediments of the Presumpscott Formation (e.g. Stuvier and Borns, 1975; Hyland, 1978; Dorion, 2001; Retelle and Weddle, 2001). Marine microfossils, shells, macroalgae and other macrofossils indicate deposition in a marine environment; consequently, we assign an indicative meaning of below MTL. A small number of terrestrial limiting points relate to organic-rich sediments or minerogenic sediments containing freshwater microfossils or macrofossils [Stuvier and Borns, 1975; Belknap et al., 1987; Anderson et al., 1992]. For these samples, we assign an indicative meaning of above highest astronomical tide.

We estimate relevant tidal datums for each sea-level indicator using the TPXO8-Atlas global tidal model [Egbert and Erofeeva, 2010]. We do not consider changes in tidal range over time; nevertheless, any such changes are likely to be small in comparison to the magnitude of the changes in relative sea level following the deglaciation of the region.

For all sea-level indicators, we account for uncertainties in the vertical position, including uncertainties related to the absolute elevation of the top of a core or section and the subsurface depth of the dated sample [Hijma et al., 2015; Khan et al., 2019]. Many of the source publications provide elevations with respect to an unspecified datum. We assume that this is mean sea level and do not apply any corrections to account for datum differences. Where possible, we derive estimates of each component of the vertical position uncertainty from the original publications and follow the recommendations of Hijma et al. [2015] where these are not stated.

Radiocarbon dating provides constraints on the age of many of the sea-level indicators in the database. We recalibrate all ages, including those in the databases of Engelhart and Horton [2012] and Vacchi et al. [2018], using OxCal v.4.2 [Bronk Ramsey, 2009] and the IntCal20 and Marine20 calibration curves [Heaton et al., 2020; Reimer et al., 2020]. To account for the marine reservoir effect, which is the difference between the age of a marine-fed organism and an atmospheric fed organism at the location of the organism, we use the *delta R* application [Reimer and Reimer, 2017] to recalculate the reservoir correction from paired terrestrial and marine samples from the Mercy Hospital landslide site (subregion 8b) [Thompson et al., 2011]. We apply the resulting correction (ΔR) of 617 ± 149 years to all marine samples older than 12 ka. Marine shells collected in the 19^{th} and 20^{th} centuries suggest a substantially smaller correction is required in the late Holocene [McNeely, 2006]. We consequently use ΔR = -70 ± 44 years from the calib 8.2 application [Stuiver et al., 2022] for data under 8 ka and linearly interpolated ΔR values for ages between 8 and 12 ka.

The subaerially exposed deltas from which we derive SLIPs lack direct age control [Thompson et al., 1989]. Nevertheless, as they were deposited in contact with the ice margin or close to it, they must have closely postdated the local deglaciation. Consequently, we are able to assign an age range with a conservative temporal uncertainty based on the timing of deglaciation. Ice-sheet recession occurred in coastal Maine starting from approximately ~14.5ka [Borns et al., 2004; Dalton et al., 2020]; we have, therefore, assigned an age of 13.5 ± 1 ka for each of these SLIPs. While falling relative sea level means that lower elevation deltas very likely postdate higher elevation deltas, uncertainties over the precise pattern and timing of the rapid retreat of ice from the region currently prevent the development of a more detailed chronology [Dalton et al., 2020].

We divide the study region into 10 subregions following the spatial partitioning adopted by Vacchi et al. [2018] for Canada and Engelhart and Horton [2012] for the United States, with further subdivision of two subregions that incorporate data from greater distances inland from the present coastline (Fig. 2.1). We plot sea-level index points as boxes with width and height proportional to the vertical and 2σ age uncertainties. We plot marine limiting points as blue T-shaped symbols and terrestrial limiting points as green ⊥-shaped symbols. For limiting points, the horizontal line lies at the extreme limit of the vertical uncertainty and the width reflects the 2σ age uncertainty.

For the assessment of the SLIPs indicating the lowstand in the Gulf of Maine, we looked into the specimen respective to all three data points. From those, one of the specimens was removed due to its damaged state suggesting the possibility of reworking. Both remaining specimens were in good condition and thus, were kept as datapoints. However, the RSL uncertainty has been increased due to rare encounters at lower depths.

2.2.2 GIA model

Assuming a spherically symmetric Earth with a Maxwell (viscoelastic) rheology, our GIA model computes the sea-level response to Late Pleistocene ice-ocean mass redistribution. This response is computed using an algorithm for 1D earth models to solve the sea-level equation. [Kendall et al., 2005; Mitrovica and Milne, 2003]. The model incorporates time-varying shorelines as well as the influence of GIA-induced changes in Earth rotation [Milne and Mitrovica, 1998; Mitrovica et al., 2005]. The two primary model inputs are an ice loading history and Earth model that defines density and rheological parameters as a function of depth.

As is common in GIA studies, the viscosity of the Earth model is partitioned into three shells: the lithosphere being the outermost region of variable thickness and high viscosity as well as the upper mantle and the lower mantle being deeper regions with uniform viscosity. The upper mantle extends from the base of the lithosphere to 670 km depth and the lower mantle extends from 670km depth to the mantle-core boundary at approximately 2891 km.

Our viscosity parameters consider multiple combinations of the following 11 upper mantle viscosity (UMV) values [0.05, 0.08, 0.1, 0.2, 0.3, 0.5, 0.8, 1, 2, 3, 5] x 10^{21} Pas and the following 10 lower mantle viscosity (LMV) values [1, 2, 3, 5, 10, 20, 30, 50, 70, 90] x 10^{21} Pas with lithosphere thickness of either 46, 71, 96 or 120 km, giving a total of 440 combinations for a single ice model, with one model run of a given combination taking up to a few minutes. The large range of viscosity parameters considered in our GIA modelling reflects the fact that the Earth's viscosity structure is not well constrained. The density and elastic structure were set according to the seismic model PREM [Dziewonski & Anderson 1981]. Within the model lithosphere, viscosity values were set to very high values (order of 10^{43} Pas) such that the viscous response is negligible on typical GIA time scales. More realistic depth-dependant viscosity values of the lithosphere (order of 10^{25} Pas) were tested by Kuchar and Milne [2015] and resulted in similar deglacial RSL responses to the simplified model considered here, except in areas under a relatively small ice sheet at LGM.

For the ice history input, we selected three published models: one developed by colleagues at the Australian National University (referred to as the ANU model hereafter) (e.g., Lambeck et al., 2014; Lambeck et al., 2017), ICE-6G [Peltier et al., 2015] as well as one North American Ice Complex history from Tarasov et al. [2012]: GLAC1D-na9927 (abbreviated to 9927 in the following). This regional model is embedded in the global ICE5G model [Peltier, 2004]. Ice extent for these models in our study region is shown at 21 ka, 17 ka and 13 ka in Figure 2.2. At 21 ka, the 9927 model has a lower ice thickness compared to ICE-6G and ANU by more than 1000 m in some areas. From 21 ka to 17 ka, all models show a significant amount of thinning, but ice remains present near the Gulf of Maine coastline. Margin retreat is greatest in the 9927 model, followed by the ICE-6G with the ANU model showing little margin retreat by 17 ka. By 13 ka, ice has retreated from the region of study in all three models. Finally, we note that the ICE-6G and 9927 models were developed assuming the viscosity model VM5a [Tarasov et al., 2012; Peltier, 2015]. The ANU model was developed via an iterative procedure to jointly optimise the Earth viscosity model and ice history, with optimum Earth model viscosity structure defined by LT=102 km, UMV=5.1 x 10^{20} Pas, LMV=1.3 x 10^{22} Pas [Lambeck et al., 2017].

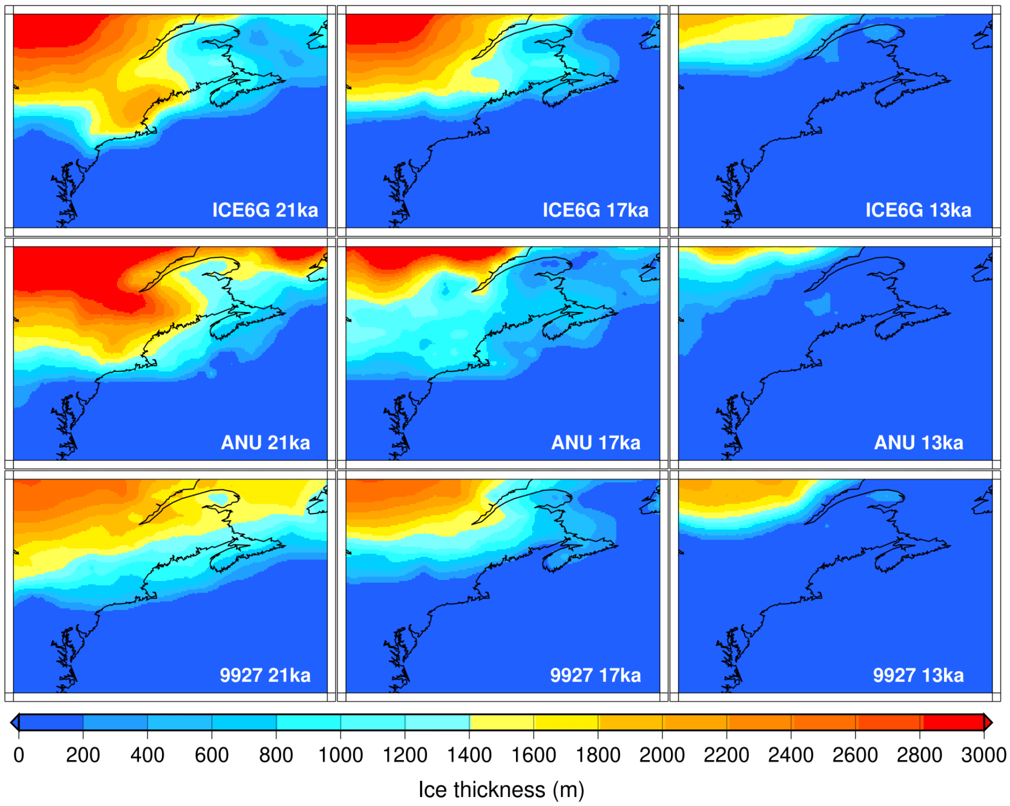

Figure 2.2 Ice thickness distributions of the ANU, ICE-6G and 9927 ice models at 21 ka, 17 ka and 13 ka for the study region.

Constraints on ice thickness changes in this region prior to major margin retreat around 15 ka are poor due to large dating uncertainties coupled with limited data to constrain margin retreat [Dalton, 2020]. Given this, we generated some relatively extreme pre-15 ka deglaciation scenarios in an attempt to fit the RSL observations. To do this, we partitioned the ICE-6G model into a regional and global component. This ice model gave some of the best results in fitting the RSL data and so it was chosen for this aspect of the model sensitivity analysis. We isolated the regional component by multiplying the ICE-6G thickness values by a disc of thickness unity which tapers to zero beyond a specified radius (see Fig. S1 and S2). The chronology of ice in this regional component (Fig. S2, inset) was varied to delay ice thinning after 21 ka and thus produce more rapid retreat near the time of rapid RSL fall around 15 ka (Fig. 2.3). The standard ICE-6G chronology was applied to ice thickness values beyond the region covered by the disc (Fig. S2, main plot). This procedure allowed us to vary the poorly known ice thickness chronology within the study region without affecting ice extent/chronology in other areas. RSL was computed for the global and regional ice models separately and these results were summed to determine the total RSL signal. The error incurred in this procedure is small (a few metres) as the RSL response is linear in the ice loading component (which dominates the RSL response in this region, see Fig. 2.7). The error is related to changes in the computed ocean loading signal which is of second order.

2.2.3 Data-model comparison

Prior to the comparison of the database with GIA models, redundant limiting data were removed using a visual analysis (see Fig. 2.3 and S3). For example, time periods with many SLIPs do not need limiting points as RSL is already well constrained via the SLIPs. Limiting data is mostly kept during periods with few or no SLIPs. In the case where two limiting points of the same type occur at the same time, only the limiting point which provides the more useful constraint is kept. For example, in the case of two lower limiting points, the one with the highest RSL value is kept to avoid redundancy (the lower point does not add additional information). The inverse applies for upper limiting points. Limiting points with the lowest uncertainty values are also prioritized as the constraint they give is more precise. As SLIPs are the most useful data type for sea-level reconstruction, all of these were kept in the data set. Removing redundant data affects the data-model comparison as the algorithm tends to give lower misfit values if the model curve respects all the redundant limiting data, which could bias our results.

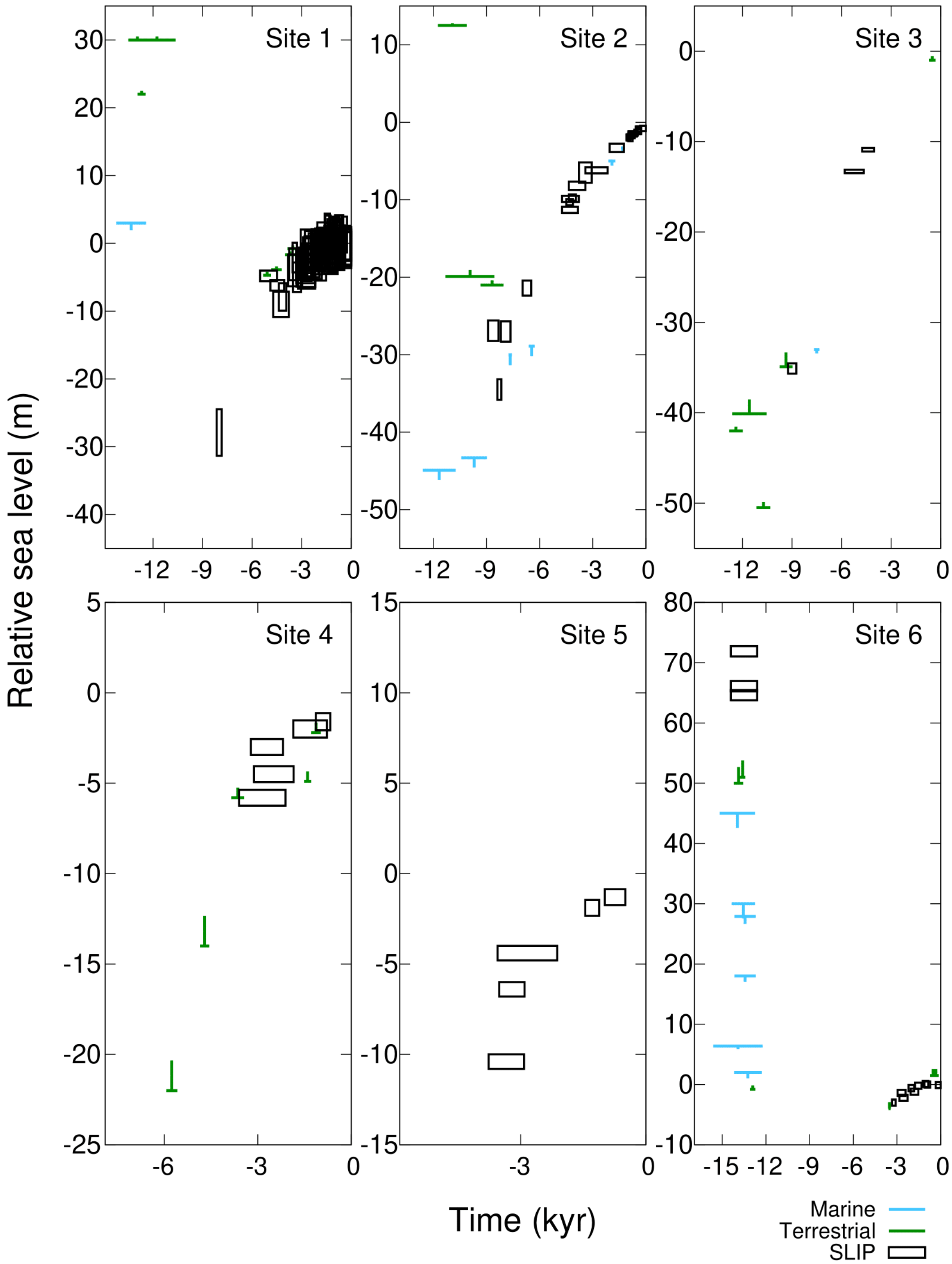

Figure 2.3 Representation of all datapoints. SLIPs are shown as black boxes, marine limiting data as blue 'T' symbols and terrestrial limiting data as inverted green 'T' symbols.

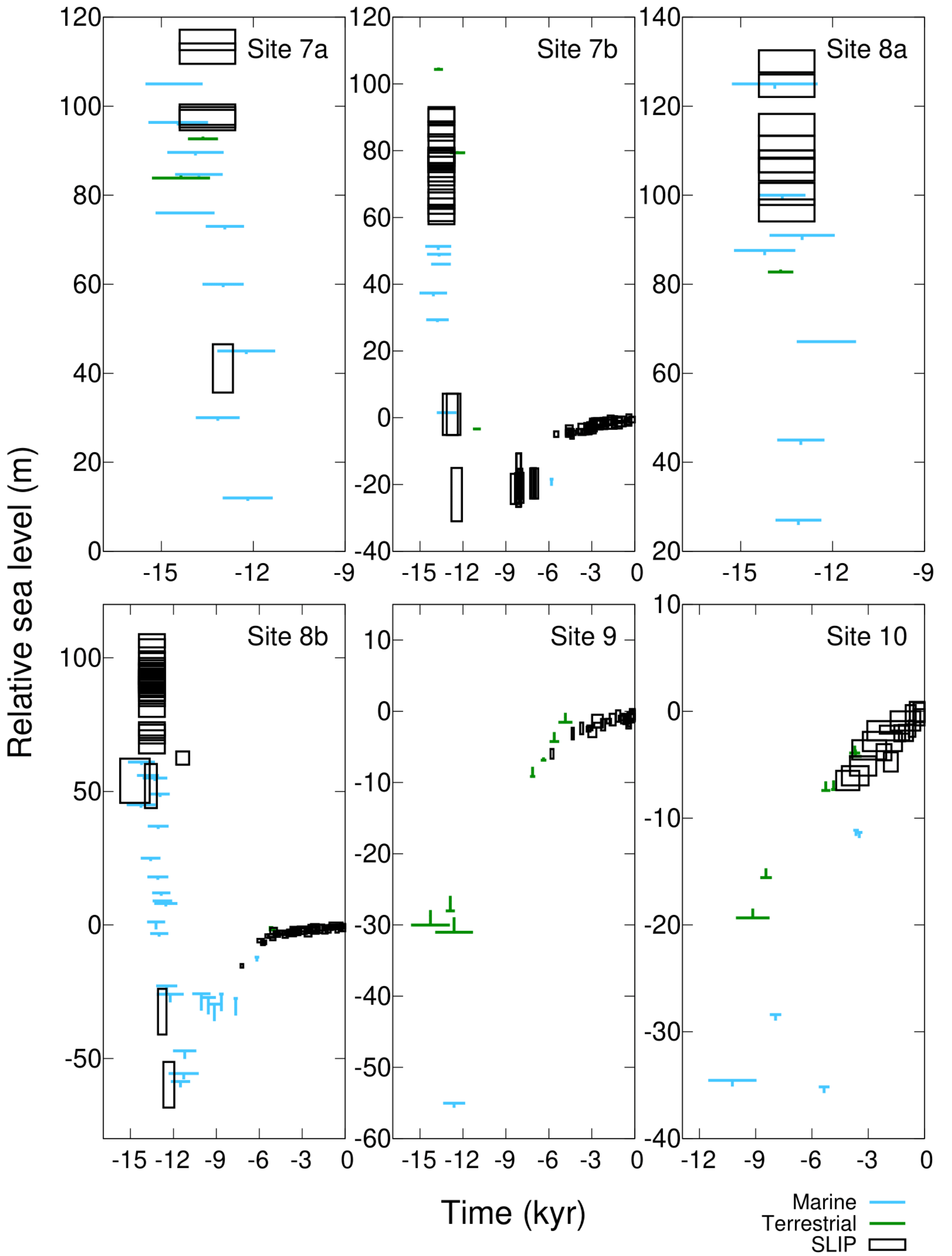

Figure. 2.3. (continued).

The quality of data-model fit for a given parameter set (i.e., set of 3 earth viscosity parameters and specified ice model) was quantified by calculating a misfit value. In total, over 1300 parameter sets were considered.

For a given parameter combination and individual SLIP location, the closest point on the model curve (in height and time) is determined. The misfit (δ_{SLIP}) is then computed using:

$$\delta_{SLIP} = \frac{\sqrt{\sum_{n=1}^{N}\left(\Delta_{RSL,n}^{2}/\sigma_{RSL,n}^{2} + \Delta_{t,n}^{2}/\sigma_{t,n}^{2}\right)}}{N} \tag{2.1}$$

With $\Delta_{RSL,n}$ and $\Delta_{t,n}$ being, respectively, the RSL and age difference between the nth observation point and the model prediction closest to this point. $\sigma_{RSL,n}$ and $\sigma_{t,n}$ are, respectively, the 2-σ observational uncertainty of the RSL and age, and N is the total number of observational data for a given subregion.

Data-model misfit for the limiting data (δ_{Lim}) were calculated differently as these data provide only a one-sided height constraint on RSL. While the SLIPs indicate that the RSL must be a specific value at a given time, the limiting data accepts any value above (for lower limiting) or below (for upper limiting) the data. Thus, finding the closest point on the model RSL curve to determine a misfit is less appropriate in this case. Therefore, model values were determined for the age of the limiting data point (including uncertainty) and a misfit calculated if the model curve sat on the 'wrong' side of the point (e.g., above an upper limiting point) using:

$$\delta_{Lim} = \frac{\sqrt{\sum_{n=1}^{N}\left(\Delta_{RSL,n}^{2}/\sigma_{RSL,n}^{2}\right)}}{N} \tag{2.2}$$

If the model value sat on the 'correct' side of the limiting point, no penalty is incurred. Since the limiting data are one-sided RSL constraints, the misfit computed is weighted by 0.5 when determining the total data-model misfit:

$$\delta_{Total} = \delta_{SLIP} + 0.5\ \delta_{Lim} \tag{2.3}$$

The Earth viscosity parameter combination giving the lowest value of δ_{Total} is selected as the best fitting viscosity model for each of the ice histories used.

2.3. Results and discussion

Our new database compiles 223 accepted sea-level indicators, of which 90 are SLIPs, 119 are marine limiting points, and 14 are terrestrial limiting points. The oldest sea-level indicators have mean ages predating 16 ka, while 93 % predate 10 ka. Of the sea-level index points, 69 are from subaerially exposed glaciomarine delta topset-foreset contacts that lack direct chronological control but must closely postdate deglaciation [Thompson et al., 1989]. Our database complements existing, predominantly post-10 ka databases compiled by Engelhart and Horton [2012] and Vacchi et al. [2018], which include 221 and 215 sea-level indicators from the region of this study, respectively. We use a compilation of 659 combined sea-level index points, terrestrial limiting points and marine limiting points from Vacchi et al. [2018], Engelhart and Horton [2012] and the new database, to reconstruct RSL for this region (Fig. 2.1).

In subregion 8b, two SLIPs constrain the depth of the lowstand (Fig. 2.1). These index points relate to articulated *Mya arenaria* and *Mytilus edulis* shells encountered in fine-grained sediments from Saco Bay, near Portland, Maine [Lee, 2006]. Tyler-Walters [2008] considers

M. edulis as intertidal to 5 m depth based on a global synthesis of records, while Suchanek [1978] reports the species to 10m below MTL along the US West coast. Similarly, *M. arenaria* is widely reported as an intertidal to shallow subtidal species [Rasmussen, 1973; Newell & Hidu, 1986; Powilleit et al., 1995]. While it has been reported from deeper depths [Theroux and Wigley, 1983], it's not clear that these specimens were live at the time of collection rather than having been reworked from their original living depths. We consequently assign indicative ranges of MTL to 10 m below MTL to both species. We reject two further samples from Lee [2006] that are from similar ages and elevations due to poor preservation of the dated shells and the possibility of reworking. We also treat a poorly preserved articulated *Modiolis modiolis* specimen as a marine limiting point due to the wide depth distribution of this species [Tyler-Walters, 2007]. The two accepted SLIPs suggest relative sea level fell from -32.5 ± 5.2 m at 12457 – 13102 cal yr BP to -59.9 ± 5.2 m at 11875 – 12710 cal yr BP. This lowstand depth is consistent with undated evidence from the submerged Kennebec palaeodelta, which features possible shorelines at elevations of -20 – -30 m, -30 – -40 m and, in its central/southern portion, -50 – -60 m [Shipp et al, 1991; Barnhardt et al., 1997]. The depth is also consistent with a fluvially incised basal unconformity observed down to an elevation of -40 m in Penobscot Bay [Knebel and Scanlon, 1985]. The basal unconformity grades into a conformity at elevations of ~ -70 – -90 m [Kelley and Belknap, 1991], suggesting that the wave base at the lowstand was above this depth.

As indicated in Fig. 2.1, the data at sites 7 and 8 were sub-divided into areas A and B. This was done because the spatial RSL gradient across these sites is large, resulting in a considerable error when including all the data on a single RSL-time plot (see Fig. S4). Partitioning the data as indicated in Fig. 2.1 reduces this error considerably. Note, that this spatial variation in the data has no impact on the misfit calculations as these values are computed at the spatial co-ordinates of each data point. It only affects the accuracy of compiling the data onto a RSL-time plot and comparing these data with a model curve (which is computed at the average of all the data points in a given area – diamonds in Fig. 2.1).

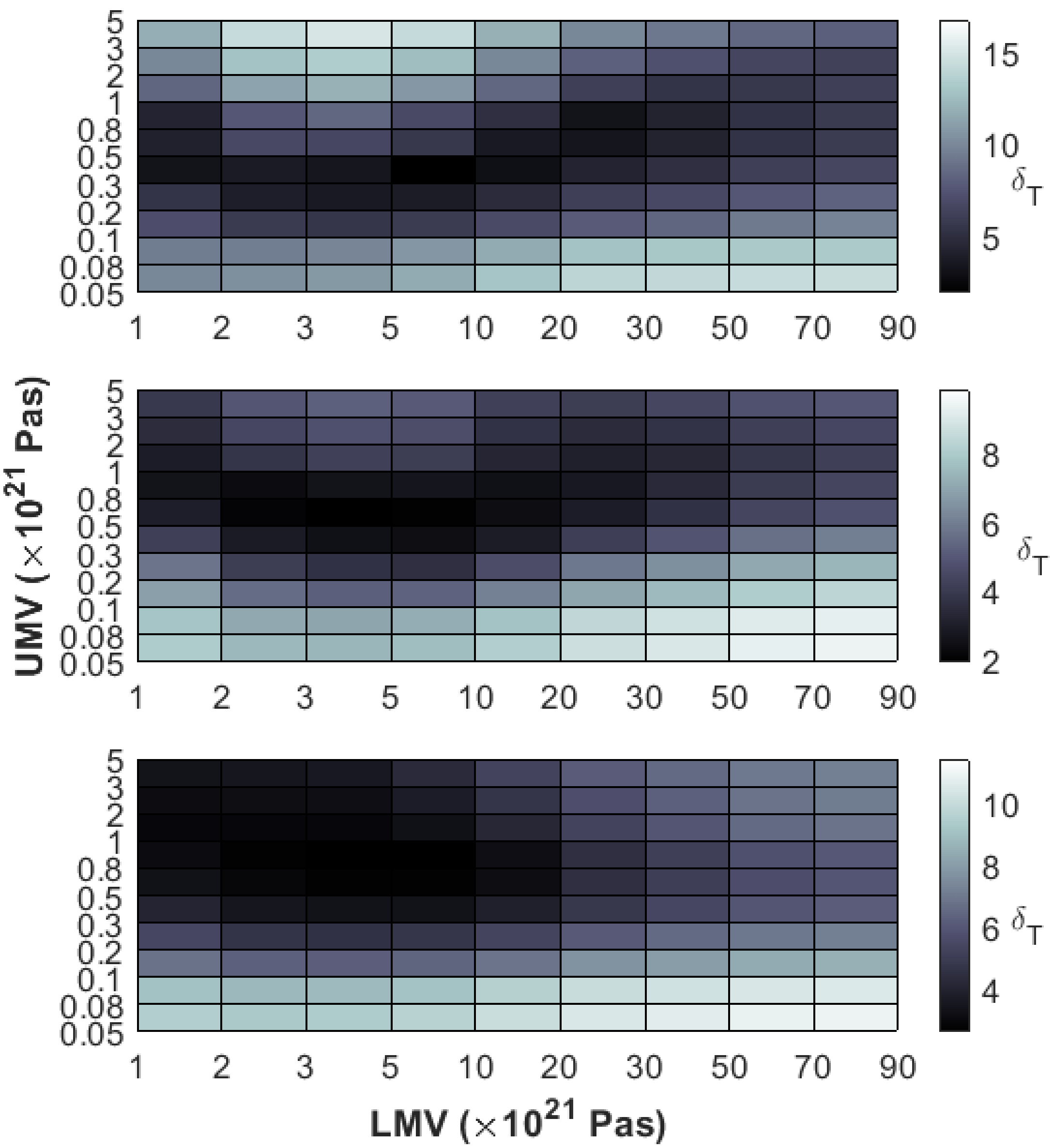

Figure 2.4 Data-model misfit value using the entire RSL data set (SLIPs and limiting data) for 11 UMV values and 10 LMV values for a given ice history and optimal lithosphere thickness: (top) LT=120 km for ICE-6G ($\boldsymbol{\delta_{min}}$=1.906 at UMV=5 x 10^{20} Pas, LMV = 5 x 10^{21} Pas), (middle) LT=120 km for ANU ($\boldsymbol{\delta_{min}}$=1.948 at UMV=8 x 10^{20} Pas, LMV = 3 x 10^{21} Pas) and (bottom) LT=46 km for 9927 ($\boldsymbol{\delta_{min}}$=2.604 at UMV=1 x 10^{21} Pas, LMV = 5 x 10^{21} Pas).

We seek to determine a model parameter set that provides a good fit to the majority of the RSL data (Fig. 2.3). In practice, this involves determining the parameters that minimise the misfit function (eqns (2.1) & (2.2)). Figure 2.4 provides a representative summary of this analysis, in which the darker areas identify the model parameters that produce the best data-model fits. The middle range of UMV values and mid to lower range of LMV values result in the best fits to our dataset. While the misfit function is broadly similar in pattern for all three ice models, there are significant differences. For example, the 9927 misfit values tend to be higher than those for ANU and ICE-6G indicating that the model fits are poorer in general for 9927. The best fits for this ice model are found for mid to low LMV values and mid to high UMV values. In comparison, the misfit functions for the ANU and ICE-6G models show a 'u-shaped' pattern of low values that results in a better constrained range of UMV and LMV values that result in optimal fits. As evident in Fig. 2.4, optimal parameter values for the ANU and ICE-6G model produce significantly better fits compared to 9927 (minimum misfit values and the Earth viscosity parameters that result in these are given in Fig. 2.4 caption). One common result for all ice models is the poor fits obtained using UMV values below 1×10^{20} Pas. Following this, we selected the set of Earth parameters with the lowest misfit value to visually compare the data to modelled RSL based on optimal parameter values for all sites.

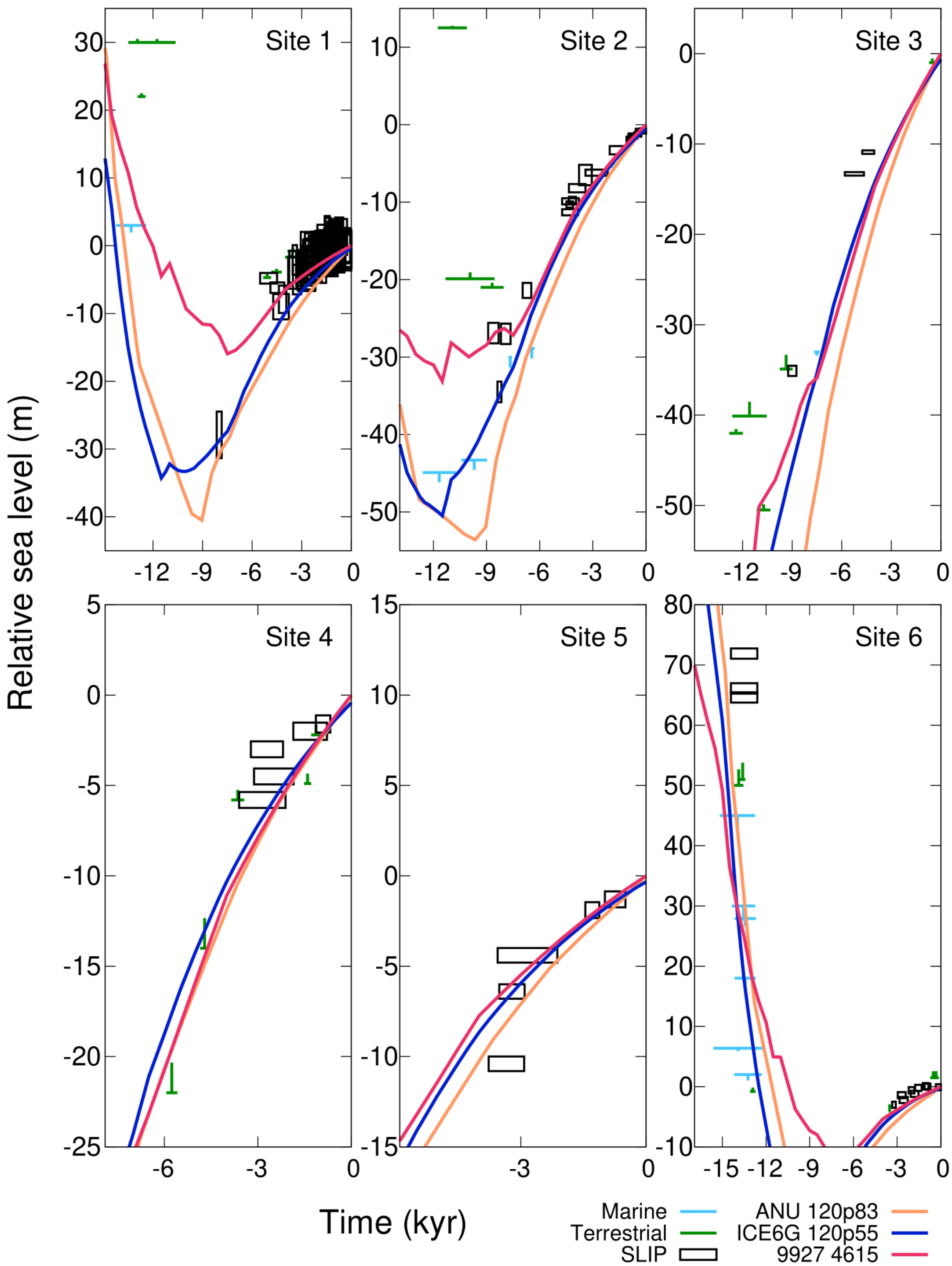

Figure 2.5 Model curves calculated at each site (diamonds in Fig. 2.1) using the parameter sets that best-fit all datapoints (solid lines). SLIPs are shown as black boxes, marine limiting data as blue 'T' symbols and terrestrial limiting data as inverted green 'T' symbols.

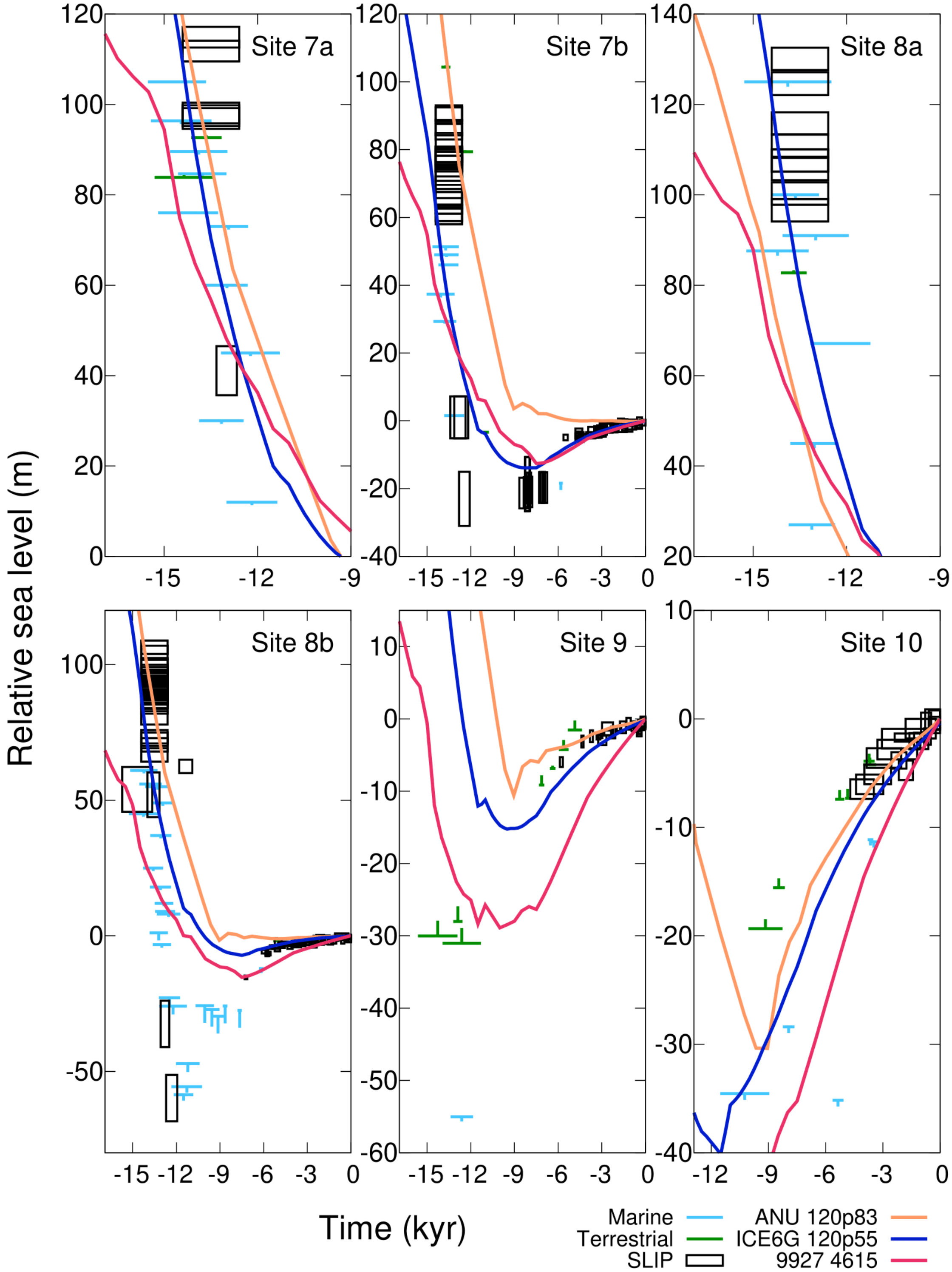

Figure. 2.5 (continued).

Model RSL curves for optimal parameter sets are plotted with the observations in Fig. 2.5. The generally higher misfit values for the 9927 ice model are evident in Fig. 2.5. For example, at site 1, the 9927 curve fits most of the data, but does not reach to the SLIP near -30m, in contrast to the ANU and ICE-6G curves. At sites 6 to 8, the 9927 model struggles to match the steep RSL fall as well as the observed lowstand. The ANU and ICE-6G models are also unable to fit the RSL fall and the depth of the lowstand, however, their predicted RSL fall is much steeper and the lowstand is deeper compared to the 9927 model. At sites 7 to 10, the 9927 model curves do not capture a lot of the younger RSL data, while the ANU and ICE-6G models do much better. In contrast, the optimal 9927 curve more closely predicts the depth of the RSL lowstand at site 9. However, the curve for 9927's optimal parameters for our region still does not reach deep enough to properly fit the lowstand near -30m. The 9927 model does fairly well at sites 2 to 5, but the fits elsewhere are of poorer quality. The ANU and ICE-6G models provide good fits at sites 1 to 6 and at site 10, hence the lower misfit values overall (Fig. 2.4). None of the models can fit the data at sites 7 to 9 where the observed RSL signal is captured most completely; a particular challenge is fitting the timing and depth of the RSL lowstand.

We also computed RSL curves using the earth viscosity models that were used in the development of ICE-6G and 9927 [VM5a Earth model; Tarasov et al., 2012; Peltier, 2015] or, for the ANU model, was the outcome of a joint inversion [Lambeck et al., 2017]. For the ANU case we used parameters that fall within the provided uncertainty ranges, specifically: LT=96 km, UMV=5×10^{20} Pas, LMV=10^{22} Pas. Unsurprisingly, the parameters determined to optimise fits to the Maine dataset (Fig. 2.4) produce better quality fits at most locations (Fig. S5).

Data-model fits were also calculated for specific sites, notably 7 and 8, to determine if significantly improved fits can be achieved at these most challenging sites. The resulting misfit plots (not shown) are similar to those obtained for the entire data set (Fig. 2.4) and so the changes in optimal parameter values for each ice model were minor. As a result there was no significant improvement in the quality of RSL fits at sites 7 and 8. As such, we adopt the optimal Earth model parameters inferred using the entire data set.

In the remainder of this section, we present a sensitivity analysis to determine the feasibility of improving the model fits to the RSL lowstand without deteriorating the fit quality elsewhere. For this analysis we focus on four sites: 6, 7b, 8b and 9. These sites were chosen because they capture, to some degree, both the glacial and Holocene aspects of the RSL response, and so are the most challenging to fit, and they span the majority of the Maine coastline.

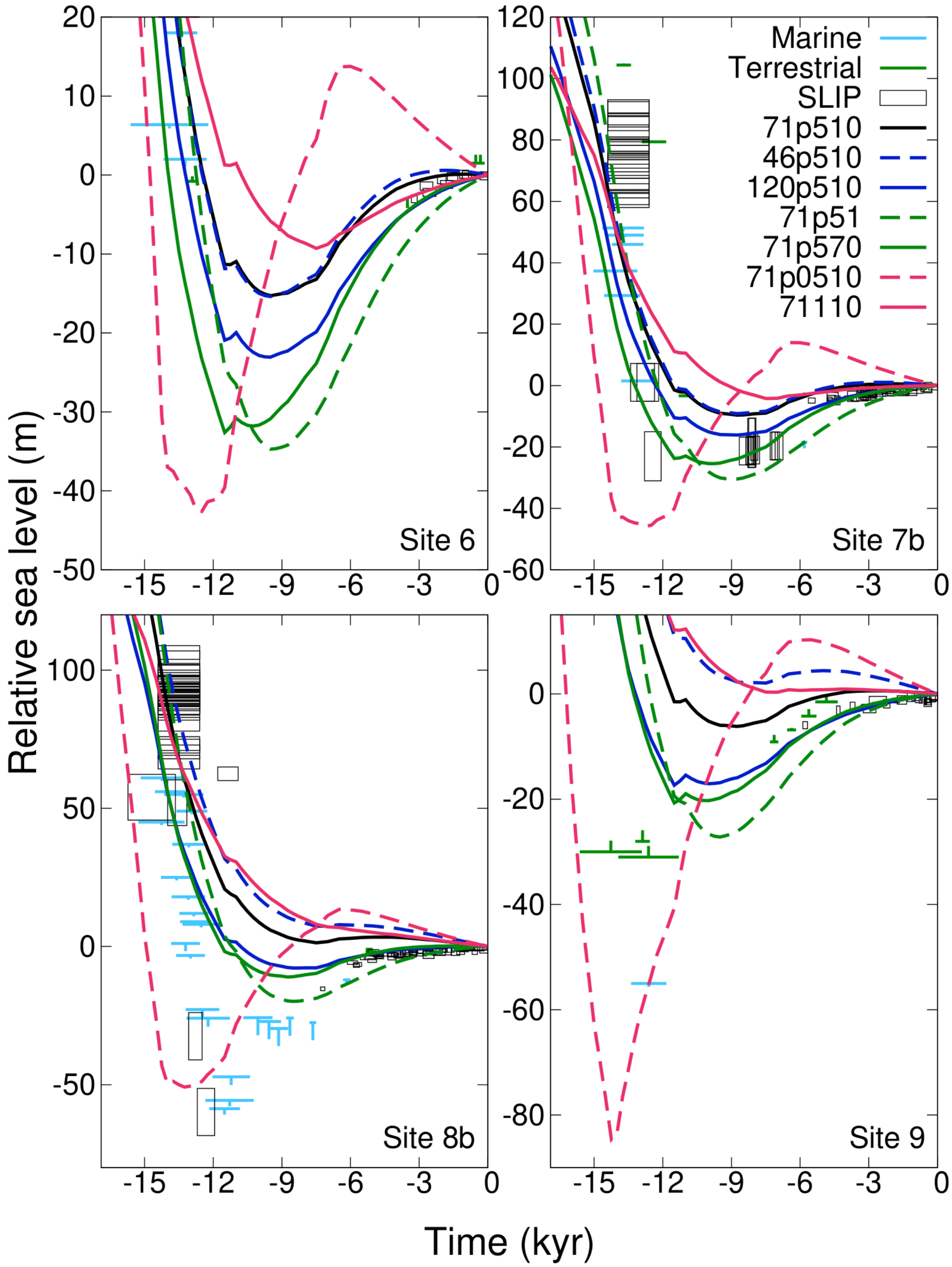

Figure 2.6 Sensitivity of the modelled RSL at sites 6, 7b, 8b and 9 to variations in lithosphere thickness (blue lines), upper mantle viscosity (pink lines) and lower mantle viscosity (green lines). The black lines indicate RSL calculated using a model with intermediate parameter values (LT=71 km, UMV=0.5 × 10^{21} Pas, LMV=10 × 10^{21} Pas; abbreviated to 71p510 in key

where viscosity values are $\times 10^{21}$ Pas and p5 stands for 0.5) which serves as a reference for the coloured lines in which one parameter value was increased (solid lines) or decreased (dashed lines) relative to the intermediate value. The ICE-6G model was used in the simulations. SLIPs are shown as black boxes, marine limiting data as blue 'T' symbols and terrestrial limiting data as inverted green 'T' symbols. See figure key for details. Note that the RSL range varies between plots.

We first consider the impact of varying the three Earth model parameter values. We define a reference parameter set that has intermediate values: LT=71 km, UMV=5×10^{20} Pas, LMV=10^{22} Pas (black line in Fig. 2.6) and vary each of the three Earth model parameters sequentially to isolate the sensitivity of modelled RSL to each one. RSL sensitivity to variation in LT indicate that thicker values result in larger RSL variations. While this is counter intuitive, it can be explained by the dominance of the ice-loading signal in this region (see Fig. 2.7 and related discussion): the thicker the lithosphere, the smaller the magnitude of ice-induced uplift (RSL fall) which leads to the barystatic signal having a larger effect and increasing the depth of the early Holocene lowstand. Model sensitivity to LMV is also significant, with variations in the order of 10s of metres. In this case, however, the intermediate curve (black line) is above both the higher and lower LMV values instead of being between them.

While both LT and LMV changes have a significant effect on the local RSL variations, the model output is most sensitive to changes in upper mantle viscosity (especially within the lower half of the range considered). A high UMV gives a similar curve to the intermediate value, but with a slightly smaller rate of change while the low UMV increases the rate of RSL change significantly. Of all the earth model parameter variations considered in Fig. 2.6, adopting a low UMV value is the only case that produces a local RSL lowstand that is broadly compatible with the data (although we note that the timing is earlier than indicated in the observations). However, the low UMV value also results in a RSL highstand during the mid-Holocene which is not observed. Based on our sensitivity analysis results for variations in LMV, we also considered model runs with low UMV values and high and low LMV values in an attempt to remove the Holocene highstand. However, similar results were obtained which we interpret as being due to a more muted sensitivity to LMV when very low UMV values are adopted, due to deformation being focused in the upper mantle region. This is compatible with the misfit results (Fig. 2.4), which indicate relatively poor-quality fits for very low UMV values (reflecting the large misfits in the mid-to-late Holocene). Thus, it appears that there is a trade-off between fitting RSL data in the late glacial and early Holocene versus fitting those in the mid-to-late Holocene.

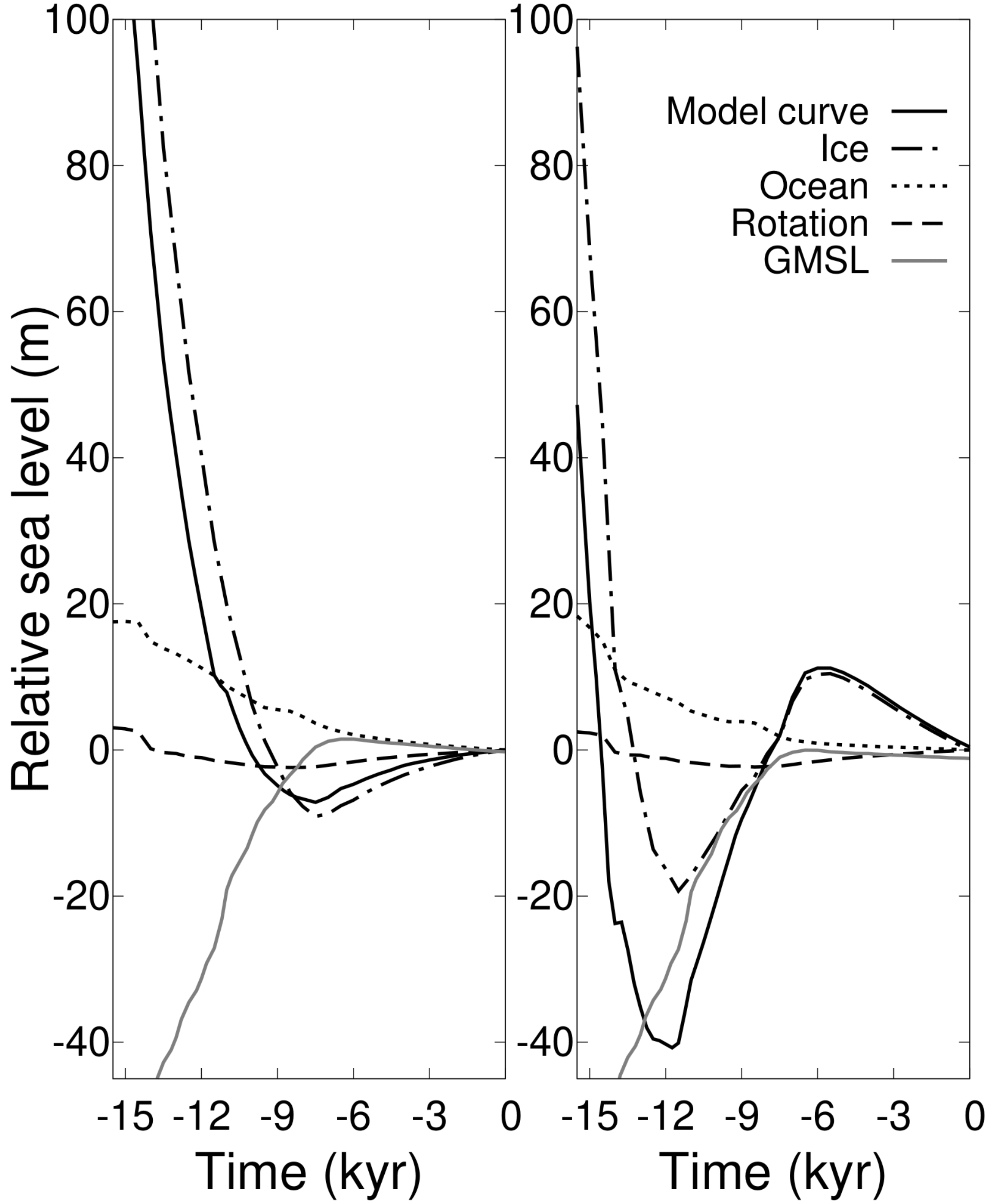

Figure 2.7 Model curves of component RSL signals (see key and main text) at site 8b for ICE-6G and Earth models (left): LT=120 km, UMV=5 x 10^{20} Pas, LMV=5 x 10^{21} Pas (these are optimal parameters for ICE-6G), and (right): as in left frame but with UMV=5 x 10^{19} Pas.

Fig. 2.7 illustrates components of the RSL model curve in the Gulf of Maine for ICE-6G and two Earth viscosity models to assist in our interpretation of the results in Fig. 2.6. Specifically, the signal associated with the ice load, ocean load, global mean changes, and due to GIA-related changes in Earth rotation are isolated at site 8b (results for other sites are similar). The global mean sea-level change includes the barystatic signal caused by the addition of melt water, and syphoning [Mitrovica and Milne, 2002]. As expected, the ice loading signal dominates the RSL response in the Gulf of Maine. This is the case regardless of the adopted ice and earth model parameters. While considerably lower in magnitude than the ice component shortly after ice retreat, the GMSL and ocean component signals are significant during the late glacial and Holocene when the ice signal has reduced in amplitude. The GMSL curve shows a large increase during deglaciation until around 7 ka, after which global melting is much reduced [e.g., Dutton et al., 2015] and so the syphoning process dominates, leading to a small RSL fall.

The ocean-loading signal contributes a RSL fall of almost 20 m since 15 ka which is dominated by subtle land uplift associated with continental levering [Clark et al., 1978]. The rotation signal does not exceed more than a few metres during deglaciation and so is not a significant contributor to the total modelled RSL. It is notable that the ocean, rotation, and GMSL signals are not strongly affected by the change in UMV (compare left and right plots in Fig. 2.7). Therefore, the large sensitivity to low UMV values found in Fig. 2.6 is strongly associated with the ice component signal. This signal includes a large RSL fall which is dominated by land uplift during deglaciation with smaller contributions from gravitational changes affecting the sea surface height. Using the optimal Earth model parameters for the ICE-6G model (left plot), the ice signal changes from a fall to a rise around 7 ka as the hinge line migrates (perpendicularly to its orientation) towards Hudson Bay resulting in the transition from land uplift to subsidence.

The ice signal for a low UMV (right plot) shows more rapid uplift and an earlier transition from (ice-induced) uplift to subsidence (~12 ka). This explains the deep and early RSL lowstand in Fig. 2.6 for UMV=5 x 10^{19} Pas. As the hinge line recedes towards Hudson Bay, this low UMV case also shows a second change in slope of the curve during the mid-Holocene which leads to the highstand around 6 ka in Fig. 2.6 for this choice of UMV. This indicates a transition from subsidence back to uplift at this time. This is suspected to be a result of channel flow in the upper mantle. As the Gulf of Maine is first situated in the near field of the ice sheet and then becomes a peripheral region during its retreat, this could explain the occurrence of a RSL Holocene highstand in a low UMV setting. Specifically, previous work [Officer et al.,1988] has shown that models with a high LMV/UMV ratio exhibit channel flow in the upper mantle which is characterised by subsidence followed by uplift of peripheral regions.

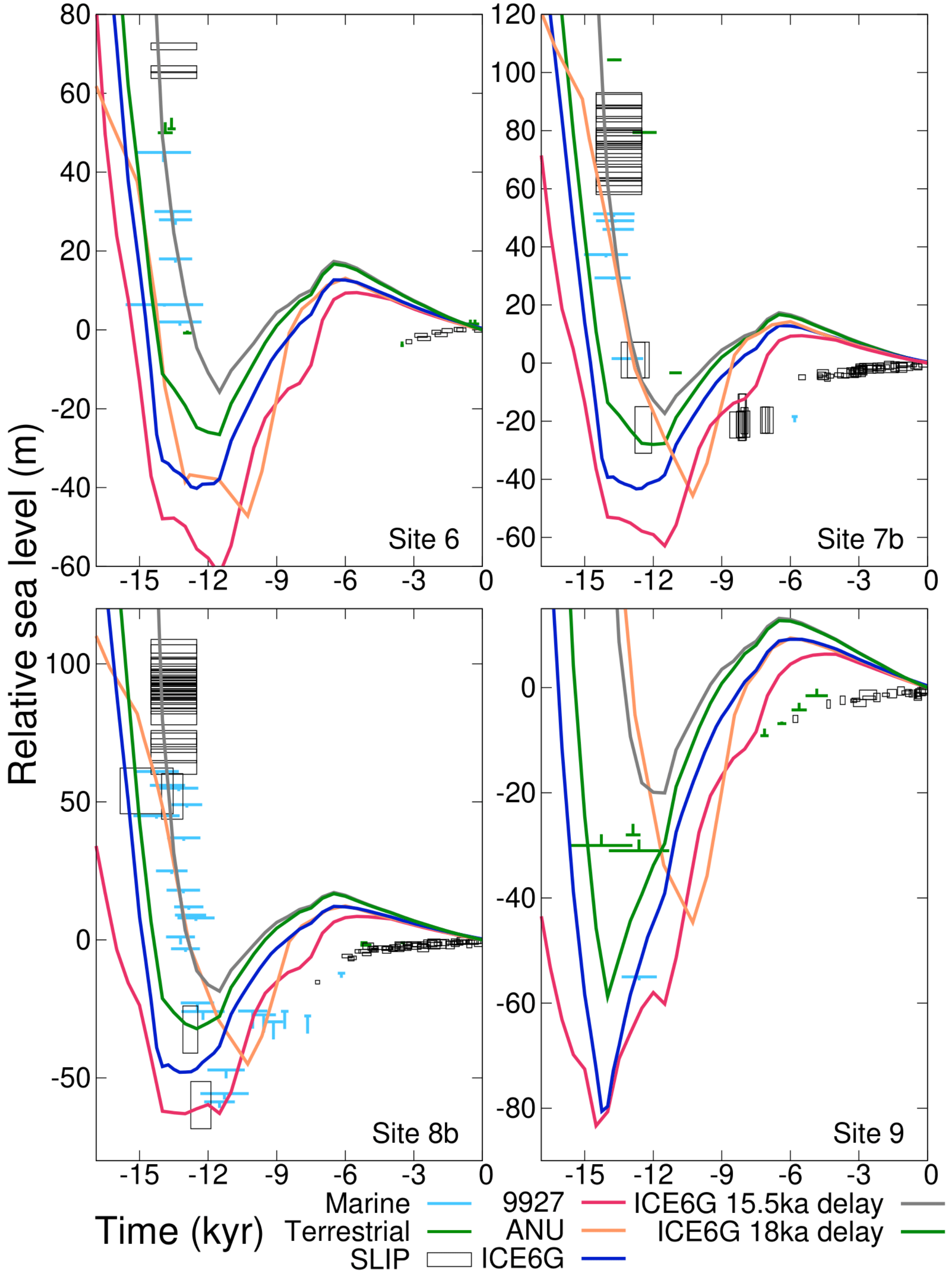

Figure 2.8 RSL model curves for various ice models for Earth viscosity parameters LT=71 km, UMV=5 x 10^{19} Pas, LMV=5 x 10^{21} Pas at sites 6 to 9. SLIPs are shown as black boxes,

marine limiting data as blue 'T' symbols and terrestrial limiting data as inverted green 'T' symbols.

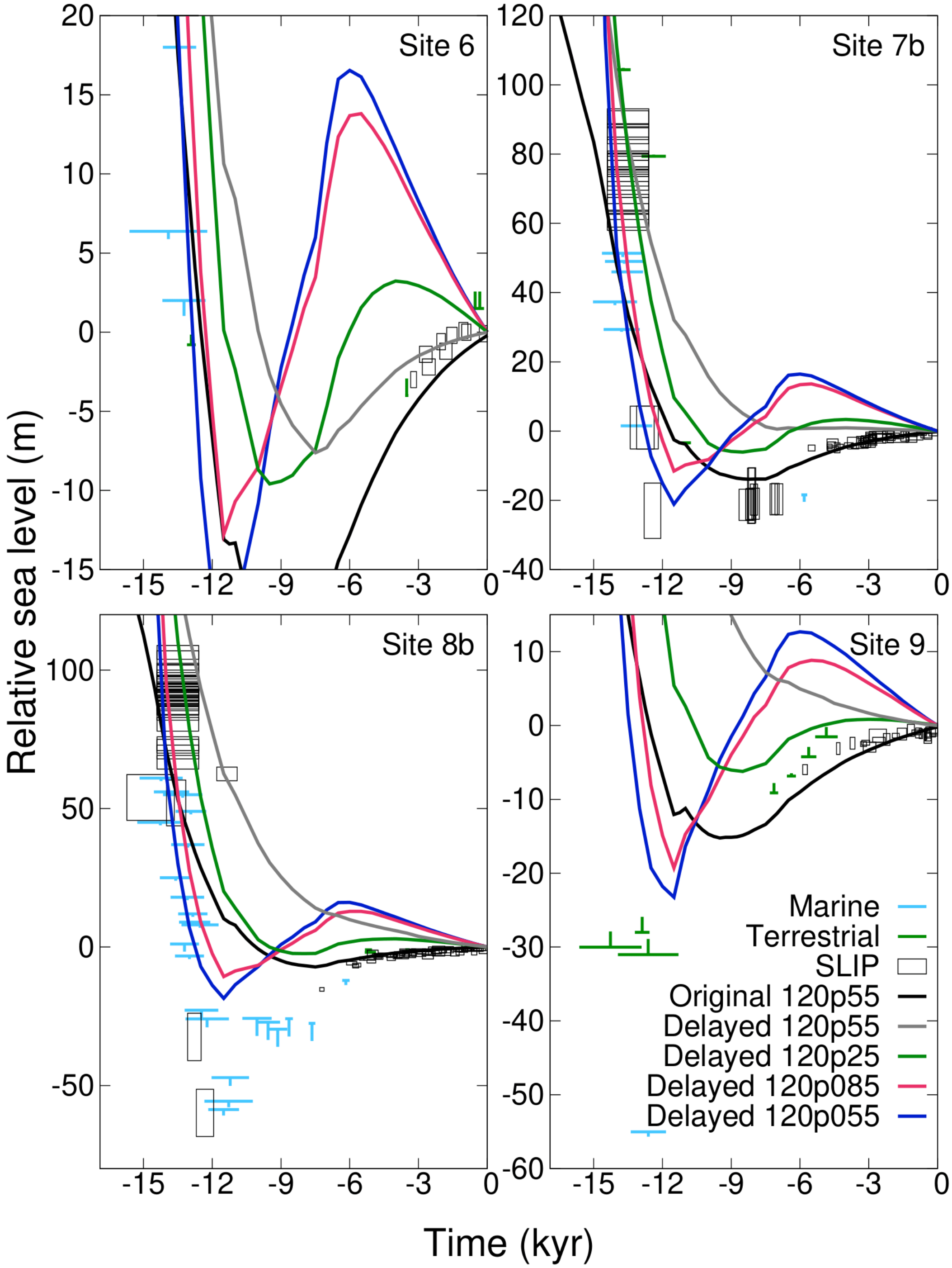

Figure 2.9 Model RSL curves at sites 6, 7b, 8b and 9 for various upper mantle viscosity values, LT=120 km, LMV=5 x 10^{21} Pas, and a late and rapid regional deglaciation of the ICE-6G model (indicated by "Delayed" in the key; see main text for more information).

SLIPs are shown as black boxes, marine limiting data as blue 'T' symbols and terrestrial limiting data as inverted green 'T' symbols.

The above results indicate that changing the Earth viscosity parameters alone cannot provide good quality fits to the RSL data, particularly at sites 7-9. To complete the sensitivity analysis, we turn our attention to the ice model to examine the sensitivity of RSL to this model input and to try and better fit the timing of the RSL fall and lowstand. As described in Section 2.2, we isolated a regional component of the ICE-6G model (Fig. S2, inset) and varied the chronology of this component only. Specifically, we considered two scenarios where the ice thickness is kept constant from 25 ka until 18 ka or 15.5 ka such that the deglaciation prior to 15 ka is later and more rapid.

Figure 2.8 shows differences between RSL curves computed using five ice models with the same set of Earth viscosity parameters (see Fig. S6 for a second set of Earth viscosity parameters). While 9927 gives deeper lowstands for this parameter set, ICE-6G gives a steeper RSL fall and so is more compatible with the older data. The ANU model gives the least steep RSL fall as well as a delayed lowstand. Both of the delayed regional deglaciation scenarios seem to give higher lowstand values with the delay until 15.5 ka giving the highest lowstand. The delay in deglaciation delays the timing of the RSL fall as well as the timing of the lowstand. Therefore, varying the timing of regional deglaciation will be necessary to improve the data-model fit with low UMV values which did not previously fit the older data (see Fig. 2.6). In general, the results in Fig. 2.8 indicate that changing the ice model governs the timing and rate of the initial RSL fall as well as the amplitude of the RSL changes. While some models are able to capture the lowstand, none are able to also match the SLIPs that define the RSL fall, particularly at site 8b. Also, all models predict a large Holocene highstand.

Of the two delayed regional scenarios, the more extreme case (15.5 ka) matched the timing of the observed RSL fall most accurately (Fig. 2.9). The delayed and more rapid deglaciation greatly improves the data-model fits for the older data, particularly at sites 7b & 8b. However, the RSL lowstand amplitude at sites 8b & 9 is further from the observed constraints (compared to results in Fig. 2.6 for low UMV viscosity case). This is somewhat counter intuitive given that the regional deglaciation is later and more rapid. However, it reflects the larger rates of barystatic RSL rise during the lateglacial period which exceeds the rate of RSL fall due to local processes, causing the RSL lowstand at ~12 ka. While there is scope to explore more deglaciation scenarios to fine tune the quality of fit to the older data, for example the timing of regional deglaciation at site 8, the misfit to Holocene data remains a key issue that cannot be resolved by varying the regional ice history. A possibility of local vertical land motion unrelated to tectonic activities has also yet to be explored.

Our efforts to fit the RSL observations using three different published ice histories, 440 combinations of viscosity parameters for a 1D (spherically symmetric) Maxwell Earth model as well as two extreme scenarios of regional deglaciation have been unsuccessful. Our results are unable to fit the rapid RSL fall immediately following deglaciation and the steady RSL rise in the mid-to-late Holocene. Matching the rapid rate of RSL fall requires low values of UMV but this leads to the prediction of a highstand in the mid-Holocene due to the large UMV-LMV contrast. Our results are based on the standard, three-layer viscosity parametrisation of the lithosphere, upper mantle and lower mantle. A different depth parametrisation of this structure could produce better fits. For example, Yousefi et al. [2018] show that adding a fourth layer to represent the asthenosphere can result in improved fits to RSL data obtained near the margin of the Cordilerran ice sheet. However, the addition of an asthenosphere did not have a strong impact in their region of study, which was also proximal to an ice margin, and so this possibility was not explored here.

Our results lead us to propose that the RSL data from Maine can be fit only by an Earth model with time dependent viscosity, such that the viscosity is weaker during large loading (stress) changes. This would provide the most effective route to fit both the older and younger data. Producing a time-varying viscosity requires the application of non-Newtonian and/or transient rheological models (e.g., Wu & Wang, 2008; Lau et al., 2021; Ivins et al., 2022; Sabadini, 1985). A recent paper by Kang et al. [2022] explores the influence of non-Newtonian rheology in the upper mantle. The results indicate a reduced UMV during deglaciation which amplifies the rate of RSL but with lower rates of vertical displacement during the Holocene when stress levels have decreased resulting in a higher effective viscosity. These characteristics indicate that this more complex model has the potential to provide good fits to the Maine data set and so we encourage future efforts to test this idea. The Maine RSL data set is arguably the best paleo record available to test and constrain the rheological component of GIA models.

2.4. Conclusions

In this study, we present an extended and critically assessed RSL data set for the Gulf of Maine. Based on our assessment of the data, we conclude that a lowstand of ~60 m along the central Maine coast is robust. However, as our database only comprises a few SLIPs to accurately constrain the extent and the timing of the lowstand, we encourage future studies to collect new data and thus help consolidate our assessment of post-glacial RSL change in this region.

Our model results are generated based on three ice histories and 440 earth models assuming a 1D (spherically symmetric) Earth with a Maxwell rheology. Results show that the models are able to bound the data at most sites relatively well, except for locations 7 and 8 where no set of model parameters is able to accurately capture the amplitude and timing of the observed RSL change. This signal is due mostly to the large influence of the ice-loading signal on the postglacial RSL response. The high rate of RSL fall can only be modelled using low values of upper mantle viscosity (order of 10^{19} Pas). However, such low viscosity values result in a mid-Holocene RSL highstand which is not supported by the observations. We also considered an extreme and delayed regional deglaciation scenario to test the sensitivity of our GIA simulations to this aspect of the ice model but were still unable to match the older and younger (Holocene) RSL observations with a single set of model parameters. We conclude that the RSL data can only be fit using more complex models of Earth rheology that can simulate changes in earth viscosity through time – via transient or non-Newtonian deformation.

2.5 Supplementary figures

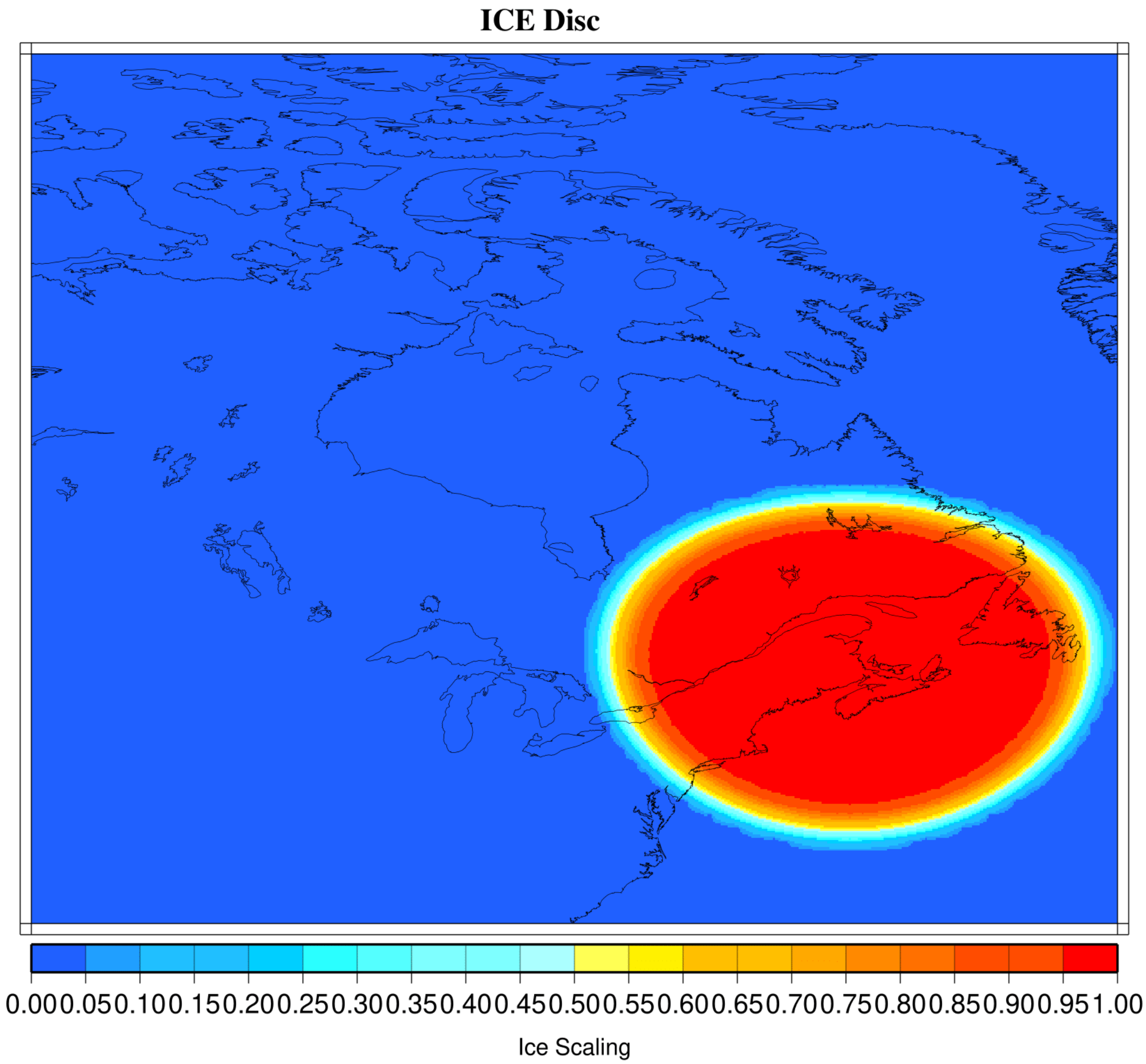

Figure S1 Representation of the ice disk varying from 1 (uniform over the region of study) to 0 (uniform outside of the region of study), before the implementation of the ice model (see Fig. S2)

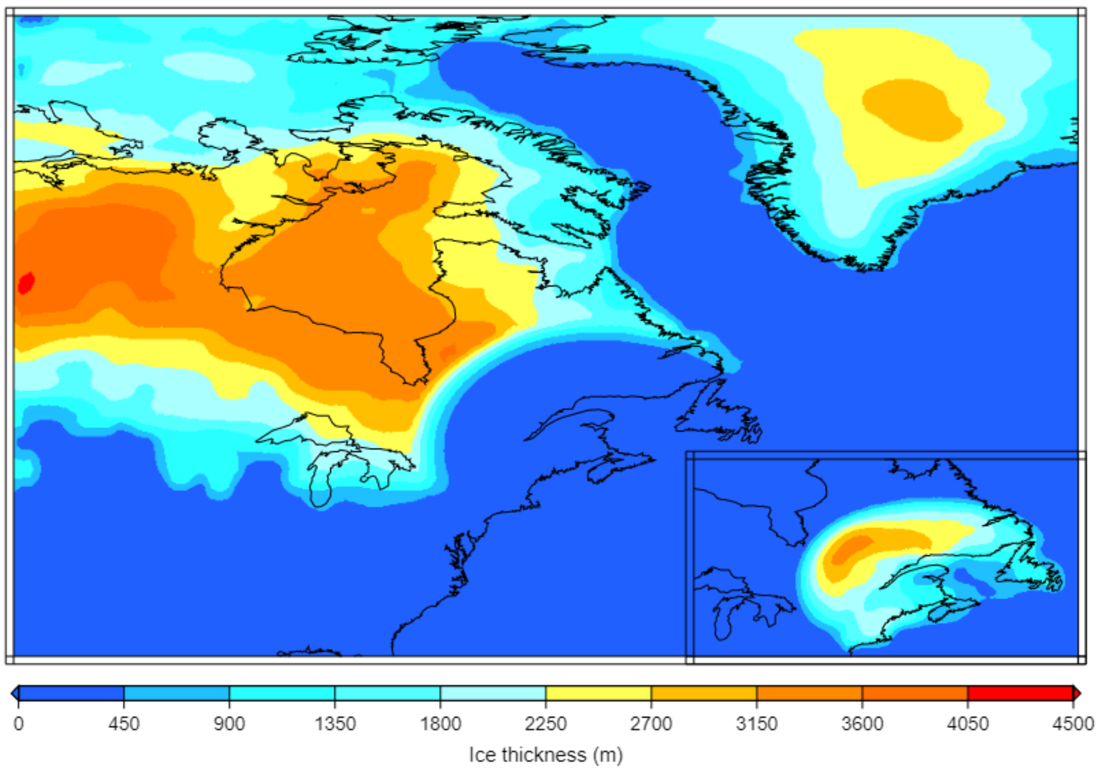

Figure S2 Representation of the global ice model and regional ice model (inset) based on ICE-6G at 21 ka.

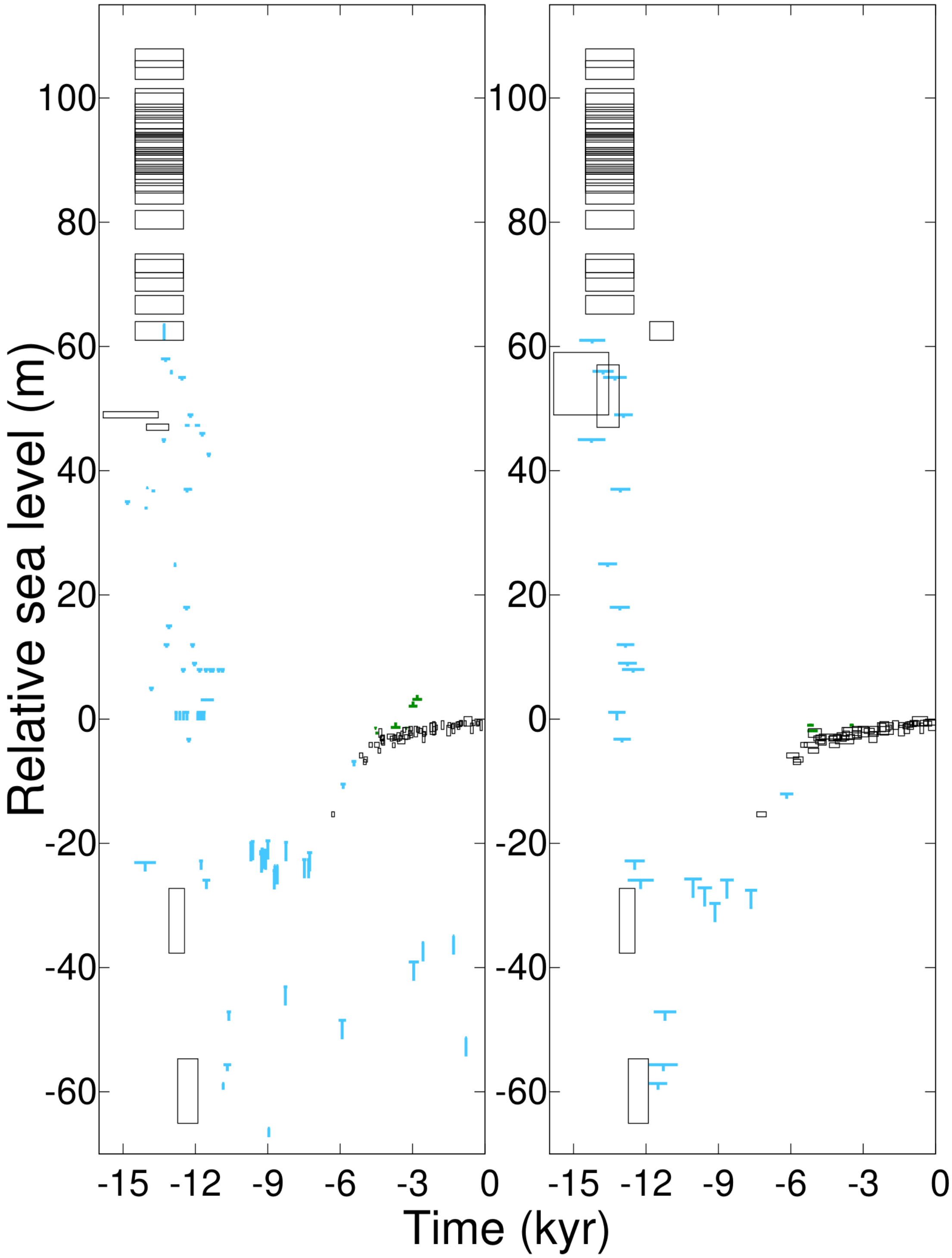

Figure S3 Representation of datapoints before cleaning and recalibration (left) and after recalibration (IntCal20 and Marine20) and cleaning (visual analysis) (right) at site 8b. SLIPs are shown as black boxes, marine limiting data as blue 'T' symbols and terrestrial limiting data as green '⊥' symbols. Note that the height uncertainty ranges for the two SLIPs that constrain the RSL lowstand were increased (as discussed in Section 3 of main text).

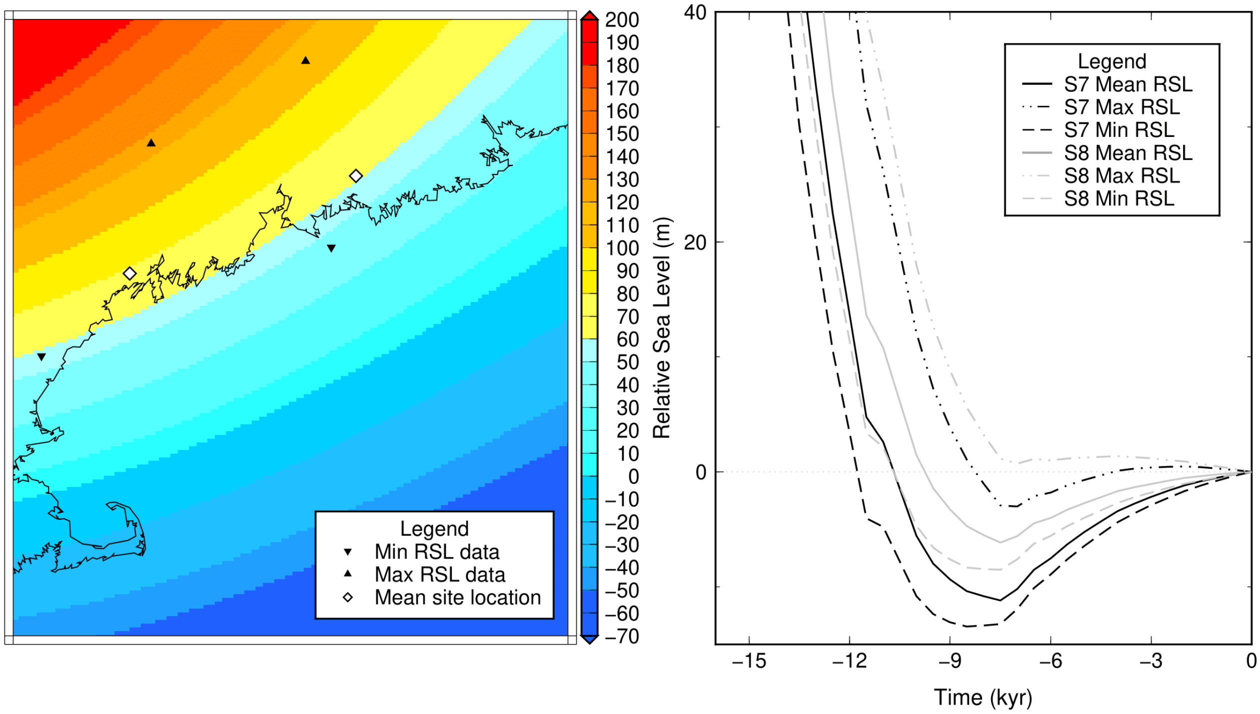

Figure S4 (Left) Model output of the RSL gradient at 14 ka for an optimal parameter set (ICE-6G, LT=120 km, UMV=5 x 10^{20} Pas, LMV = 5 x 10^{21} Pas) with selected datapoint locations from sites 7 & 8 that indicate the RSL range spanned by the data (see figure key). (Right) RSL model curves at minimum and maximum locations at sites 7 & 8 (defined via the map on left) as well as the mean location determined from all data at each site.

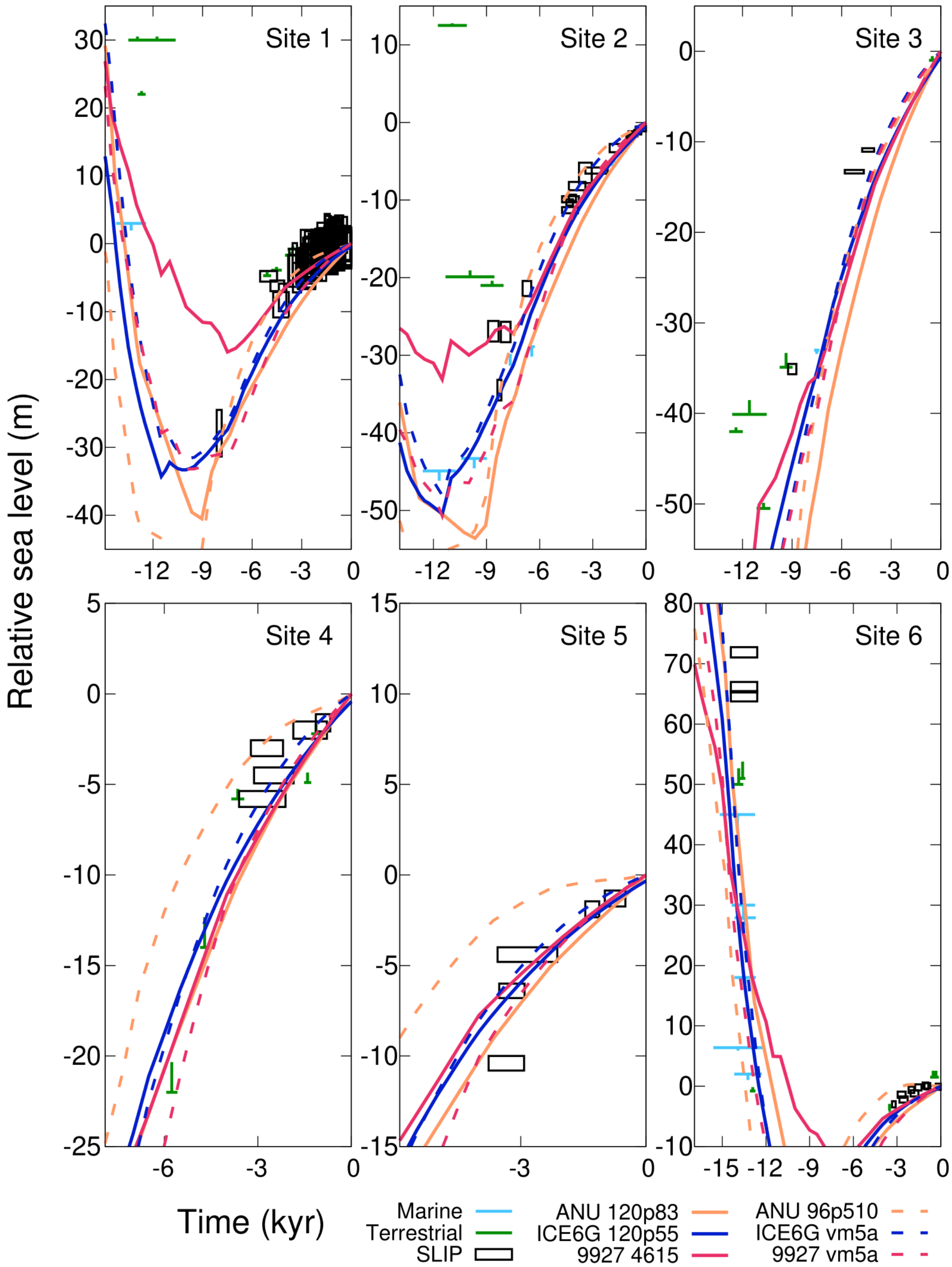

Figure S5 Model curves calculated at each site (diamonds in Fig. 2.1) using the parameter sets that best-fit all datapoints (solid lines) and each ice model's partner viscosity parameters (dashed lines). SLIPs are shown as black boxes, marine limiting data as blue 'T' symbols and terrestrial limiting data as inverted green 'T' symbols.

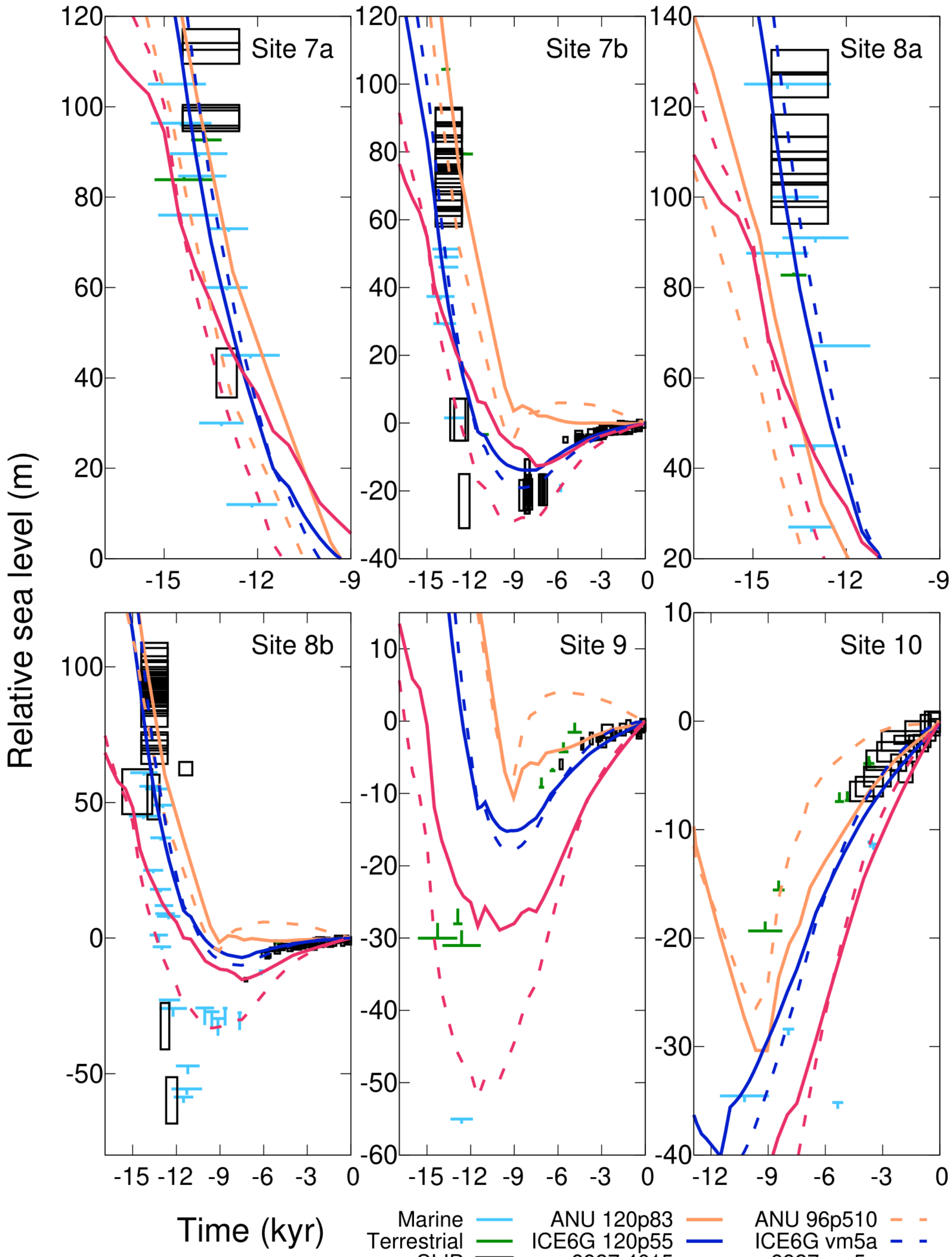

Figure. S5 (continued).

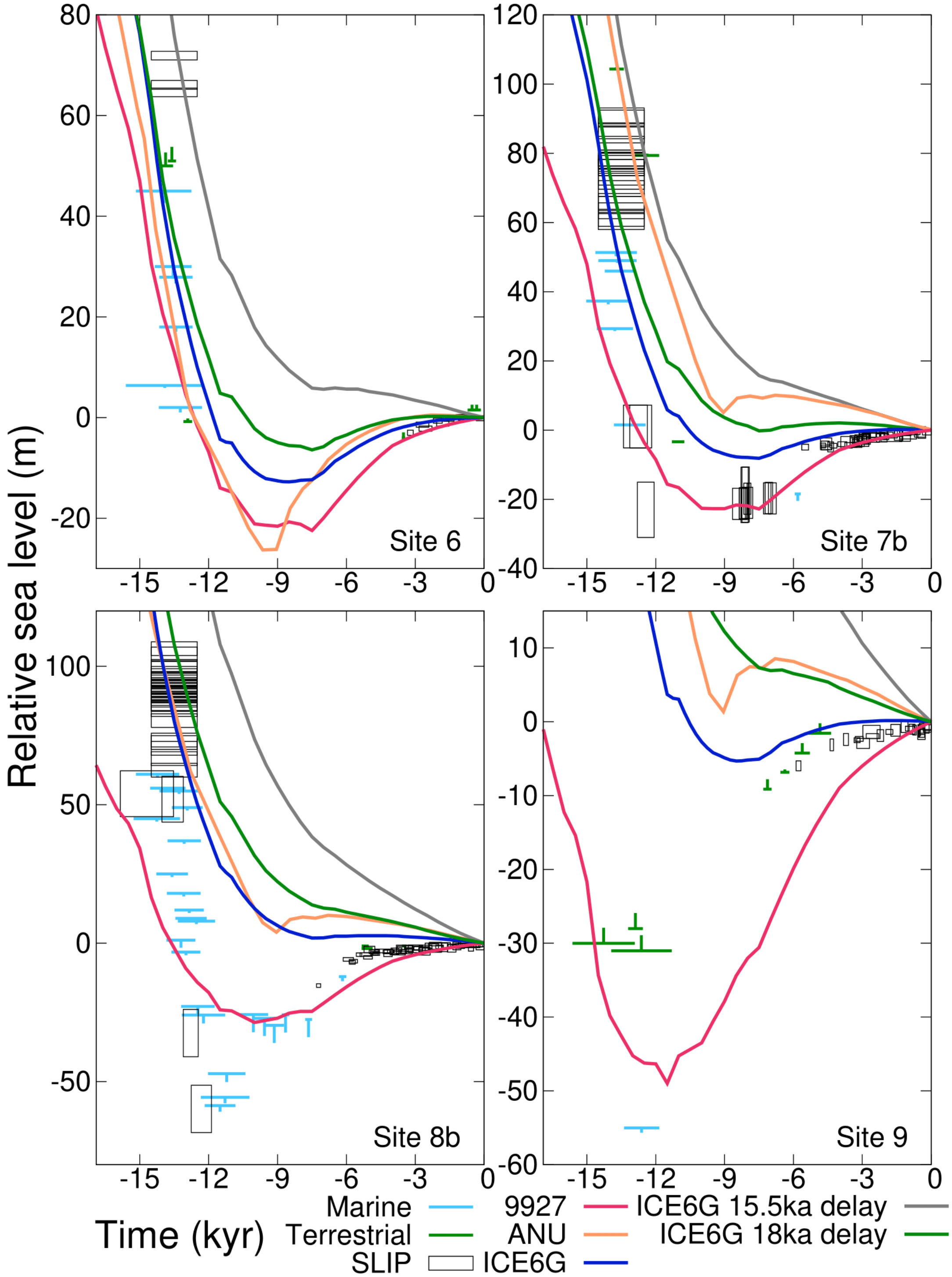

Figure S6 RSL model curves for various ice models for Earth viscosity parameters LT=71 km, UMV=5 x 10^{20} Pas, LMV=5 x 10^{21} Pas at sites 6 to 9. SLIPs are shown as black boxes, marine limiting data as blue 'T' symbols and terrestrial limiting data as inverted green 'T' symbols.

Chapter 3. Conclusion

As past ice sheet deglaciation proved that GIA is a process that can trigger large RSL changes (around 100 m scale) in just a few kyr, GIA modelling has been one of the key components in RSL studies in the past few decades. In fact, significant progress has been made by incorporating GIA to research on the rheology of the Earth as well as global and regional ice sheet history [Whitehouse, 2018]. In this thesis, we compared GIA model predictions to a critically assessed database from the region of Maine in order to better understand past sea-level history as well as the regional rheology.

The research presented in this thesis was able to fulfil the aims defined in Section 1.1. The accuracy of the paleo data composing the RSL reconstruction in the Gulf of Maine was assessed. All samples that were either poorly preserved or subject to possible reworking were removed from the database. Remaining samples of articulated Mya arenaria and Mytilus edulis shells that indicate a lowstand around -60 m were investigated through reports about the natural habitat of those species relative to sea level (e.g., Rasmussen, 1973; Suchanek, 1978; Theroux and Wigley, 1983; Tyler-Walters, 2008). As there have been some rare occurrences of finding these species at lower depths than thought when the RSL lowstand was originally reconstructed, the RSL uncertainty range was increased on these SLIPs. Since few samples were found to indicate the lowstand, geomorphic features were also used to corroborate the depth of the lowstand, which confirmed the assessment, improving the knowledge of the past RSL changes in this region. That said, given the low number of samples available to quantify the lowstand, future work to consolidate the value determined in this study is recommended.

Using the revised database, a GIA model was thoroughly tested using a set of 440 Earth parameter combinations and five different ice histories. While data-model misfit analysis showed a preference for mid to low LMV values and mid range UMV values, no combination of Earth parameters and/or ice history was able to generate a model curve that fit the large amplitude and timing of the RSL reconstruction in the Gulf of Maine. The modelled RSL curve is most sensitive to variations in UMV. Specifically, low UMV values (order of 10^{19} Pas) were able to provide a large amplitude RSL fall similar to the one observed in the region but occurring too soon compared to the data. This is compatible with the fact that the ice-loading signal is dominant in the late glacial period and early Holocene. An extreme and delayed regional deglaciation scenario was able to provide a better timing for the RSL fall and lowstand, however the lowstand amplitude was underpredicted due to the larger barystatic signal at this later time. These attempts at fitting the rapid RSL fall and lowstand using low UMV parameters resulted in a predicted RSL highstand during the mid-Holocene which is not observed. Thus, it appears that there is a trade-off between fitting RSL data in the late glacial and early Holocene versus fitting those in the mid-to-late Holocene.

Based on our results, we conclude that a single set of Earth and ice parameters cannot fit RSL observations all throughout deglaciation to the present time. While changing the three-layer viscosity parametrisation to a four-layer one by adding the asthenosphere could help improve the fits, previous tests from a near field location indicate that this solution is not likely have a strong impact on the results. However, exploring this possibility would be a useful addition to our results. The nature of our data-model misfits imply that an Earth model with time dependent viscosity, such that the viscosity is weaker during large loading (stress) changes, would be able to match the observations using a single model parameter set. Future work should, therefore, include a more complex rheology (transient and/or non-Newtonian) that can simulate changes in viscosity through time.

The Maine RSL data set is arguably the best paleo record available to test and constrain the rheological component of GIA models. The dataset provides a close to continuous regional record since ice retreated around 15 ka and is located on a passive margin so that tectonic contributions to RSL are negligible. As coastal Maine is located in a transition zone between the near-field and the peripheral region of a past major ice sheet, the RSL signal is large and complex, thus providing a stringent test for GIA models. As such, our revised dataset will play an important role in further testing and constraining models of the GIA process, particularly the Earth component of these models.

As the Greenland and Antarctica ice sheets are still present to this day and have entered a deglaciation phase, GIA models are used to predict the global sea-level response at present and into the future. Thus, the improvements in these models through their comparison with paleo data sets will lead to better predictions of future RSL changes throughout the globe. More specifically, predictions of the spatial variation of RSL changes related to GIA could prove useful to implant solutions to protect coastal cities against sea-level changes and flooding.

References

Ablain, M., Legeais, J.F., Prandi, P. et al. Satellite Altimetry-Based Sea Level at Global and Regional Scales. Surv Geophys 38, 7–31 (2017). https://doi.org/10.1007/s10712-016-9389-8

Anderson E.C., Arnold J.R., Libby W.F. (1951). Measurement of Low Level Radiocarbon. Review of Scientific Instruments 22, 225-230, https://doi.org/10.1063/1.1745896

Anderson, R.S., Jacobson Jr, G.L., Davis, R.B., Stuckenrath, R. (1992). Gould Pond, Maine: late-glacial transitions from marine to upland environments. Boreas 21, 359–371.

Ara Begum R., Lempert R., Ali E., Benjaminsen T.A., Bernauer T., Cramer W., Cui X., Mach K., Nagy G., Stenseth N.C., Sukumar R., and Wester P. (2022). Point of Depaarture and Key Concepts. In: Climate Change 2022: Impacts, Adaptation, and Vulnerability. Contribution of Working Group II to the Sixth Assessment Report of the Intergovernmental Panel on Climate Change [Pörtner H.-O., Roberts D.C., Tignor M., Poloczanska E.S., Mintenbeck K., Alegría A., Craig M., Langsdorf S., Löschke S., Möller V., Okem A., Rama B. (eds.)]. Cambridge University Press. In Press.

Barnett R.L., Bernatchez P., Garneau M. and Juneau M.-N. (2017), Reconstructing late Holocene relative sea-level changes at the Magdalen Islands (Gulf of St. Lawrence, Canada) using multi-proxy analyses. J. Quaternary Sci., vol.32 p.380-395. https://doi.org/10.1002/jqs.2931

Barnhardt, W.A., Belknap, D.F., Kelley, J.T. (1997). Stratigraphic evolution of the inner continental shelf in response to late Quaternary relative sea-level change, northwestern Gulf of Maine. Geological Society of America Bulletin 109, 612–630.

Barnhardt, W.A., Roland Gehrels, W., Kelley, J.T. (1995). Late Quaternary relative sea-level change in the western Gulf of Maine: Evidence for a migrating glacial forebulge. Geology 23, 317–320.

Becker B., Kromer B. (1993) The continental tree-ring record — absolute chronology, 14C calibration and climatic change at 11 ka. Palaeogeography, Palaeoclimatology, Palaeoecology, Vol 103, Issues 1–2, P. 67-71, ISSN 0031-0182, https://doi.org/10.1016/0031-0182(93)90052-K

Belknap, D.F., Andersen, B.G., Anderson, R.S., Anderson, W.A., Borns, H.W., Jacobson, G.L., Kelley, J.T., Shipp, R.C., Smith, D.C., Stuckenrath, R. (1987). Late Quaternary sea-level changes in Maine, in: Sea-Level Fluctuation and Coastal Evolution. SEPM Society for Sedimentary Geology 41.

Bennett C.L., Beukens R.P., Clover M.R., Gove H.E., Liebert R.B., Litherland A.E., Purser K.H., Sondheim W.E. (1977). Radiocarbon Dating Using Electrostatic Accelerators: Negative Ions Provide the Key. Science, vol. 198, 4316, p. 508-510, doi: 10.1126/science.198.4316.508

Berglund, M. (1992). Shore level changes during the Late Weichselian deglaciation in Halland, southwestern Sweden. Geologiska Föreningen i Stockholm Förhandlingar 114, 395–415.

Bernstein A., Gustafson M.T. & Lewis R. (2019) Disaster on the horizon: The price effect of sea level rise, Journal of Financial Economics, Volume 134, Issue 2, 2019,Pages 253-272, ISSN 0304-405X, https://doi.org/10.1016/j.jfineco.2019.03.013.

Borns Jr, H.W., Doner, L.A., Dorion, C.C., Jacobson Jr, G.L., Kaplan, M.R., Kreutz, K.J., Lowell, T. V, Thompson, W.B., Weddle, T.K. (2004). The deglaciation of Maine, USA, in: Developments in Quaternary Sciences. Elsevier, pp. 89–109.

Bronk Ramsey, C., 2009. Bayesian analysis of radiocarbon dates. Radiocarbon 51, 337–360.

Butzin, M., Köhler, P., and Lohmann, G. (2017), Marine radiocarbon reservoir age simulations for the past 50,000 years, Geophys. Res. Lett., 44, 8473– 8480. https://doi.org/10.1002/2017GL074688

Cazenave, A., Champollion, N., Benveniste, J. et al. (2017) International Space Science Institute (ISSI) Workshop on Integrative Study of the Mean Sea Level and its Components. Surv Geophys 38, 1–5. https://doi.org/10.1007/s10712-016-9402-2

Chappell, J. (1974). Geology of Coral Terraces , Huon Peninsula , New Guinea : A Study of Quaternary Tectonic Movements and Sea-Level Changes. Geological Society of America Bulletin 85, 553–570.

Church, J.A., P.U. Clark, A. Cazenave, J.M. Gregory, S. Jevrejeva, A. Levermann, M.A. Merrifield, G.A. Milne, R.S. Nerem, P.D. Nunn, A.J. Payne, W.T. Pfeffer, D. Stammer and A.S. Unnikrishnan (2013) Sea Level Change. In: Climate Change 2013: The Physical Science Basis. Contribution of Working Group I to the Fifth Assessment Report of the Intergovernmental Panel on Climate Change [Stocker, T.F., D. Qin, G.-K. Plattner, M. Tignor, S.K. Allen, J. Boschung, A. Nauels, Y. Xia, V. Bex and P.M. Midgley (eds.)]. Cambridge University Press, Cambridge, United Kingdom and New York, NY, USA, pp. 1137–1216, https://doi.org/10.1017/CBO9781107415324.026

Clark J.A., Farrell W.E., Peltier W.R. (1978). Global changes in postglacial sea level: A numerical calculation. Quaternary Research, Vol. 9, Issue 3, P. 265-287, ISSN 0033-5894, https://doi.org/10.1016/0033-5894(78)90033-9

Cook, C. T., & van der Plicht, J. (2007). Radiocarbon Dating: Conventional method. Encyclopedia of Quaternary Science, 2007, 2899-2911. https://doi.org/10.1016/B0-44-452747-8/00040-5

Dalton A.S., Margold M., Stokes C.R., Tarasov L., Dyke A.S., Adams R.S., Allard S., Arends H.E., Atkinson N., Attig J.W., Barnett P.J., Robert L. Barnett R.L., Batterson M., Bernatchez P., Borns H.W., Breckenridge A., Briner J.P., Brouard E., Campbell J.E., Carlson A.E., Clague J.J., Curry B.B., Daigneault R.-A., Dubé-Loubert H., Easterbrook D.J., Franzi D.A., Friedrich H.G., Funder S., Gauthier M.S., Gowan A.S., Harris K.L., Hétu B., Hooyer T.S., Jennings C.E., Johnson M.D., Kehew A.E., Kelley S.E., Kerr D., King E.L., Kjeldsen K.K., Knaeble A.R., Lajeunesse P., Lakeman T.R., Lamothe M., Larson P., Lavoie M., Loope H.M., Lowell T.V., Lusardi B.A., Manz L., McMartin I., Nixon F.C., Occhietti S., Parkhill M.A., Piper D.J.W., Pronk A.G., Richard P.J.H., Ridge J.C., Ross M., Roy M., Seaman A., Shaw J., Stea R.R., Teller J.T., Thompson W.B., Thorleifson L.H., Utting D.J., Veillette J.J., Ward B.C., Weddle T.K., Wright H.E. (2020). An updated radiocarbon-based ice margin chronology for the last deglaciation of the North American Ice Sheet Complex, Quaternary Science Reviews, vol. 234, 106223, ISSN 0277-3791. https://doi.org/10.1016/j.quascirev.2020.106223

Dutton A., Carlson A., Long A., Milne G.A., Clark P., DeConto R., Horton B., Rahmstorf S., Raymo M. (2015). SEA-LEVEL RISE. Sea-level rise due to polar ice-sheet mass loss during past warm periods. Science (New York, N.Y.). vol. 349, p. aaa4019. https://doi.org/10.1126/science.aaa4019

Dziewonski, A. & Anderson, D. (1981). Preliminary reference earth model, Phys. Earth planet. Inter., 25, 297–356.

Egbert, G.D., Erofeeva, S.Y. (2010). The OSU TOPEX/Poseiden Global Inverse Solution TPXO. Oregon State University.

Engelhart S.E., Peltier W.R., Horton B.P. (2011). Holocene relative sea-level changes and glacial isostatic adjustment of the U.S. Atlantic coast. Geology vol. 39 (8) p. 751–754. https://doi.org/10.1130/G31857.1

Engelhart, S. E., & Horton, B. P. (2012). Holocene sea level database for the Atlantic coast of the United States. Quaternary Science Reviews, 54, 12–25. https://doi.org/10.1016/j.quascirev.2011.09.013

Farrell W.E., Clark J.A. (1976). On Postglacial Sea Level. Geophysical Journal International, Vol. 46, Issue 3, P. 647–667, https://doi.org/10.1111/j.1365-246X.1976.tb01252.x

Fernlund, J.M.R. (1988). The deglaciation sea level and the marine limit in the Laholm—Halmstad area, Sweden. Geologiska Föreningen i Stockholm Förhandlingar 110, 207–220.

Furrer, R., Sain, S.R., Nychka, D. et al. (2007) Multivariate Bayesian analysis of atmosphere–ocean general circulation models. Environ Ecol Stat 14, 249–266. https://doi.org/10.1007/s10651-007-0018-z

Gardner J.V., Armstrong A.A., Calder B.R. & Beaudoin J. (2014) So, How Deep Is the Mariana Trench?, Marine Geodesy, 37:1, 1-13, https://doi.org/10.1080/01490419.2013.837849

Garola A., López-Dóriga U., Jiménez J.A. (2022) The economic impact of sea level rise-induced decrease in the carrying capacity of Catalan beaches (NW Mediterranean, Spain), Ocean & Coastal Management, Volume 218, 2022, 106034, ISSN 0964-5691, https://doi.org/10.1016/j.ocecoaman.2022.106034.

Gebbie G. (2020). Cancelation of Deglacial Thermosteric Sea Level Rise by a Barosteric Effect. Journal of Physical Oceanography 50, 12: 3623-3639. https://doi.org/10.1175/JPO-D-20-0173.1

Gobo, K., Ghinassi, M., Nemec, W. (2015). Gilbert-type deltas recording short-term base-level changes: Delta-brink morphodynamics and related foreset facies. Sedimentology 62, 1923–1949.

Gomez, N., Pollard, D., Mitrovica, J. X., Huybers, P., & Clark, P. U. (2012). Evolution of a coupled marine ice sheet–sea level model. Journal of Geophysical Research: Earth Surface, 117(F1). https://doi.org/10.1029/2011JF002128

Gornitz, V. (1995) Monitoring sea level changes. Climatic Change 31, 515–544. https://doi.org/10.1007/BF01095160

Gregory J.M., Griffies S.M., Hughes C.W. et al. (2019) Concepts and Terminology for Sea Level: Mean, Variability and Change, Both Local and Global. Surv Geophys 40, 1251–1289. https://doi.org/10.1007/s10712-019-09525-z

Haaf, L., Watson, E.B., Elsey-Quirk, T. et al. Sediment Accumulation, Elevation Change, and the Vulnerability of Tidal Marshes in the Delaware Estuary and Barnegat Bay to Accelerated Sea Level Rise. Estuaries and Coasts 45, 413–427 (2022). https://doi.org/10.1007/s12237-021-00972-9

Han, H.K., Gomez, N., Pollard, D. and DeConto, R.. (2021). Modeling Northern Hemispheric ice sheet dynamics, sea level change and solid Earth deformation through the last glacial cycle. J. Geophys. Res.: Earth Surface. 125, 4, e2020JF006040

http://dx.doi.org/10.1029/2020JF006040

Hijma, M.P., Engelhart, S.E., Törnqvist, T.E., Horton, B.P., Hu, P., Hill, D.F. (2015). A protocol for a geological sea-level database. Handbook of Sea-Level Research, edited by: Shennan, I., Long, AJ, and Horton, BP, Wiley Blackwell 536–553.

Hinkel, J., Aerts, J.C.J.H., Brown, S. et al. (2018) The ability of societies to adapt to twenty-first-century sea-level rise. Nature Clim Change 8, 570–578. https://doi.org/10.1038/s41558-018-0176-z

Ivins E.R., Caron L., Adhikari S., Larour E. (2022). Notes on a compressible extended Burgers model of rheology, Geophysical Journal International, Vol. 228, Issue 3, P.1975–1991, https://doi.org/10.1093/gji/ggab452

James, T.S., Hutchinson, I., Barrie, J.V., Conway, K.W., Mathews, D. (2005). Relative sea-level change in the northern Strait of Georgia, British Columbia. Géogr. Phys. Quaternaire 59, 113-127. https://doi.org/10.7202/014750ar

James, T.S., Gowan, E.J., Wada, I., Wang, K. (2009). Viscosity of the asthenosphere from glacial isostatic adjustment and subduction dynamics at the northern Cascadia subduction zone, British Columbia, Canada. J. Geophys. Res. 114 https://doi.org/10.1029/2008JB006077

Jebbad R., Pau Sierra J., Mösso C., Mestres M. & Sánchez-Arcilla A. (2022) Assessment of harbour inoperability and adaptation cost due to sea level rise. Application to the port of Tangier-Med (Morocco), Applied Geography, Volume 138, 102623, ISSN 0143-6228, https://doi.org/10.1016/j.apgeog.2021.102623.

Jull, A. J. T. (2013). AMS Radiocarbon Dating. In Encyclopedia of Quaternary Science: Second Edition (pp. 316-323). Elsevier Inc.. https://doi.org/10.1016/B978-0-444-53643-3.00044-3

Kang K., Zhong S., Geruo A., Mao W. (2022) The effects of non-Newtonian rheology in the upper mantle on relative sea level change and geodetic observables induced by glacial isostatic adjustment process, Geophysical Journal International, Vol. 228, Issue 3, P. 1887–1906. https://doi.org/10.1093/gji/ggab428

Kelley, J.T., Belknap, D.F. (1991). Physiography, surficial sediments and Quaternary stratigraphy of the inner continental shelf and nearshore region of the Gulf of Maine. Continental Shelf Research 11, 1265–1283.

Kelley J.T., Belknap D.F., Claesson S. (2010) Drowned coastal deposits with associated archaeological remains from a sea-level "slowstand": Northwestern Gulf of Maine, USA. Geology, vol. 38 (8) p.695–698. https://doi.org/10.1130/G31002.1

Kemp A.C., Horton B.P., Donnelly J.P., Mann M.E., Vermeer M., Rahmstorf S. (2011) Climate related sea-level variations over the past two millennia. Proceedings of the National Academy of Sciences, vol.108 (27) p.11017-11022 https://doi.org/10.1073/pnas.1015619108

Kendall, R.A., Mitrovica, J.X., Milne, G.A. (2005). On post-glacial sea level-II. Numerical formulation and comparative results on spherically symmetric models. Geo.phys. J. Int. 161 (3), 679–706. https://doi.org/10.1111/j.1365-246X.2005.02553.x

Khan, N.S., Ashe, E., Shaw, T.A. et al.(2015) Holocene Relative Sea-Level Changes from Near-, Intermediate-, and Far-Field Locations. Curr Clim Change Rep 1, p.247–262. https://doi.org/10.1007/s40641-015-0029-z

Khan N.S., Horton B.P., Engelhart S., Rovere A., Vacchi M., Ashe E.L., Törnqvist T.E., Dutton A., Hijma M.P., Shennan I. (2019). Inception of a global atlas of sea levels since the Last Glacial Maximum. Quaternary Science Reviews, Vol. 220, P. 359-371, ISSN 0277-3791, https://doi.org/10.1016/j.quascirev.2019.07.016.

Klos A., Kusche J., Fenoglio-Marc L. et al. (2019) Introducing a vertical land motion model for improving estimates of sea level rates derived from tide gauge records affected by earthquakes. GPS Solut 23, 102. https://doi.org/10.1007/s10291-019-0896-1

Knebel, H.J., Scanlon, K.M. (1985). Sedimentary framework of Penobscot Bay, Maine. Marine Geology 65, 305–324.

Kuchar J. and Milne G.A. (2015) The influence of viscosity structure in the lithosphere on predictions from models of glacial isostatic adjustment. Journal of Geodynamics, vol. 86, pp. 1–9. https://doi.org/10.1016/j.jog.2015.01.002

Lambeck K., Rouby H., Purcell A., Sun Y., Sambridge M. (2014). Sea level and global ice volumes from the Last Glacial Maximum to the Holocene. Proceedings of the National Academy of Sciences, Vol. 111 (43), P. 15296-15303. https://www.pnas.org/doi/abs/10.1073/pnas.1411762111

Lambeck, K., Purcell, A. and Zhao, S. (2017). The North American Late Wisconsin ice sheet and mantle viscosity from glacial rebound analyses. Quaternary Science Reviews, 158, 172-210. https://doi.org/10.1016/j.quascirev.2016.11.033

Lau H.C.P., Austermann J., Holtzman B.K., Havlin C., Lloyd A.J., Book C., & Hopper E. (2021). Frequency dependent mantle viscoelasticity via the complex viscosity: Cases from Antarctica. Journal of Geophysical Research: Solid Earth, 126, e2021JB022622. https://doi.org/10.1029/2021JB022622

Lee, K. (2006), Late Quaternary sea-level lowstand environments and chronology of outer Saco Bay, Maine. MSc thesis, University of Maine.

Ling S.J., Sanny J., Moebs W. (2016). University Physics Volume 3. Houston, Texas. OpenStax. https://openstax.org/books/university-physics-volume-3/pages/1-introduction

Love, R., Milne, G.A., Tarasov, L., Engelhart, S.E., Hijma, M.P., Latychev, K., Horton, B.P. and Törnqvist, T.E. (2016), The contribution of glacial isostatic adjustment to projections of sea-level change along the Atlantic and Gulf coasts of North America. Earth's Future, 4: 440-464. https://doi.org/10.1002/2016EF000363

Lowe, J.J., & Walker, M. (2014). Reconstructing Quaternary Environments (3rd ed.). Routledge. https://doi.org/10.4324/9781315797496

Macinnis-Ng, Cate et al. (2021) Climate-change impacts exacerbate conservation threats in island systems: New Zealand as a case study, Front Ecol Environ 2021; 19(4): 216– 224, https://doi.org/10.1002/fee.2285

Martin-Español A., King M. A., Zammit-Mangion A., Andrews S. B., Moore P., and Bamber J. L. (2016), An assessment of forward and inverse GIA solutions for Antarctica, J. Geophys. Res. Solid Earth, 121, 6947– 6965, https://doi.org/10.1002/2016JB013154

McNeely, R., Dyke, A.S., Southon, J.R. (2006), Canadian marine reservoir ages preliminary data assessment. Geological Survey of Canada.

Milne G.A., Mitrovica J.X. (1998). Postglacial sea-level change on a rotating Earth. Geophys. J. Int. 133 (1), 1–19. https://doi.org/10.1046/j.1365-246X.1998.1331455.x

Milne G.A., Mitrovica J.X.(2008) Searching for eustasy in deglacial sea-level histories. Quaternary Science Reviews, Vol. 27, Issues 25–26, Pages 2292-2302, ISSN 0277-3791. https://doi.org/10.1016/j.quascirev.2008.08.018

Milne, G., Gehrels, W., Hughes, C. et al. (2009) Identifying the causes of sea-level change. Nature Geosci 2, 471–478. https://doi.org/10.1038/ngeo544

Milne G.A., Peros M. (2013). Data–model comparison of Holocene sea-level change in the circum-Caribbean region.Global and Planetary Change,Vol. 107, P. 119-131, ISSN 0921-8181, https://doi.org/10.1016/j.gloplacha.2013.04.014

Milne, G.A. & Shennan, I.. (2013). Isostasy: Glaciation-Induced Sea-Level Change. Encyclopedia of Quaternary Science. 452-459. https://doi.org/10.1016/B978-0-444-53643-3.00135-7

Milne, G. A. (2015) Sea Level. Coastal Environments and Global Change, Chichester, West Sussex ; Hoboken, NJ : American Geophysical Union, John Wiley & Sons, 2014. p. 28-51. https://doi.org/10.1002/9781119117261.ch2

Milne G.A.. (2015). Glacial isostatic adjustment. https://doi.org/10.1002/9781118452547.ch28

Mitrovica J.X., Milne G.A. (2002) On the origin of late Holocene sea-level highstands within equatorial ocean basins. Quaternary Science Reviews, Vol. 21, Issues 20–22, P. 2179-2190, ISSN 0277-3791, https://doi.org/10.1016/S0277-3791(02)00080-X.

Mitrovica,J.X.,Milne, G.A. (2003). On post-glacial sea level:I. General theory. Geophys. J. Int. 154 (2), 253–267. https://doi.org/10.1046/j.1365-246X.2003.01942.x

Mitrovica, J.X., Wahr, J., Matsuyama, I., Paulson, A. (2005). The rotational stability of an ice-age Earth. Geophys. J. Int. 161, 491–506. https://doi.org/10.1111/j.1365-246X.2005.02609.x

Moczo P., Kristek J. & Franek P. (2006). Lecture Notes on Rheological Models. Comenius University, Faculty of Mathematics, Physics and Informatics, Department of Astronomy, Physics of the Earth, and Meteorology.

Muscheler, R. and Heikkilä, U. (2011). Constraints on long-term changes in solar activity from the range of variability of cosmogenic radionuclide records, Astrophysics and Space Sciences Transactions, vol. 7, no. 3, p. 355–364. doi:10.5194/astra-7-355-2011.

Nelson D.E., Korteling R.G., Stott W.R.(1977). Carbon-14: Direct Detection at Natural Concentrations. Science, Vol. 198, 4316, p.507-508, doi: 10.1126/science.198.4316.507

Newell, C.R., Hidu, H. (1986), Species profiles: Life histories and environmental requirements of coastal fish and invertebrates (North Atlantic): Softshell clam.[Mya arenaria]. Maine Shellfish Research and Development, Damariscotta (USA); Maine University.

Obolewski, K., Piesik, Z. (2005), Mya arenaria (L.) in the Polish Baltic Sea coast (Kołobrzeg–Władysławowo). Baltic Coastal Zone 9, Institute of Biology and Environmental Protection, Pomeranian Pedagogical University, Słupsk.

O'Brien, K. (1979), Secular variations in the production of cosmogenic isotopes in the Earth's atmosphere, J. Geophys. Res., 84(A2), 423– 431, doi:10.1029/JA084iA02p00423.

Officer, C. B., Newman, W. S., Sullivan, J. M., and Lynch, D. R. (1988). Glacial isostatic adjustment and mantle viscosity, J. Geophys. Res., 93(B6), 6397– 6409, https://doi.org/10.1029/JB093iB06p06397

Park, E., Loc, H.H., Van Binh, D. et al. (2022) The worst 2020 saline water intrusion disaster of the past century in the Mekong Delta: Impacts, causes, and management implications. Ambio 51, 691–699. https://doi.org/10.1007/s13280-021-01577-z

Peltier W.R., Andrews J.T. (1976). Glacial-Isostatic Adjustment—I. The Forward Problem, Geophysical Journal International, Vol. 46, Issue 3, P. 605-646. https://doi.org/10.1111/j.1365-246X.1976.tb01251.x

Peltier, W. R., Yuen, D. A., and Wu, P. (1980) Postglacial rebound and transient rheology. Geophysical Research Letters, vol. 7, no. 10, pp. 733–736. https://doi.org/10.1029/GL007i010p00733.

Peltier, W.. (1999). Global sea level rise and glacial isostatic adjustment. Global and Planetary Change- GLOBAL PLANET CHANGE. 20. 93-123. https://doi.org/10.1016/S0921-8181(98)00066-6

Peltier, W.R. (2004). Global glacial isostasy and the surface of the ice-age Earth: the ICE-5G(VM2) model and GRACE. Annu. Rev. Earth Planet. Sci. 2004 (32),111-149. https://doi.org/10.1146/annurev.earth.32.082503.144359

Peltier, W. R., D. F. Argus, D.F. and R. Drummond (2015). Space geodesy constrains ice-age terminal deglaciation: The global ICE-6G C(VM5a) model. J. Geophys. Res. Solid Earth, 120, 450-487, https://doi.org/10.1002/2014JB011176

Powilleit, M., Kube, J., Maslowski, J., Warzocha, J. (1995), Distribution of macrobenthic invertebrates in the Pomeranian Bay (southern Baltic) in 1993/94. Bull. Sea Fish. Inst., Gdynia 3, 75–87.

Purser K.H., Liebert R.B., Litherland A.E., Beukens R.P., Gove H.E., Bennett C.L., Clover M.R. and Sondheim W.E. (1977). An attempt to detect stable N- ions from a sputter ion source and some implications of the results for the design of tandems for ultra-sensitive carbon analysis. Rev. Phys. Appl. (Paris), 12 10, 1487-1492 doi: 10.1051/rphysap:0197700120100148700

Quarta G, Maruccio L, D'Elia M, Calcagnile L. (2021) Radiocarbon Dating of Marine Samples: Methodological Aspects, Applications and Case Studies. Water.; 13(7):986. https://doi.org/10.3390/w13070986

Rasmussen, E. (1973), Systematics and ecology of the Isefjord marine fauna (Denmark) with a survey of the eelgrass (Zostera) vegetation and its communities. Ophelia 11, 1–507.

Reimer P.J., Reimer R.W. (2007) RADIOCARBON DATING | Calibration. Encyclopedia of Quaternary Science, Elsevier, P. 2941-2950, ISBN 9780444527479, https://doi.org/10.1016/B0-44-452747-8/00045-4.

Reimer, R., & Reimer, P. (2017). An Online Application for ΔR Calculation. Radiocarbon, 59(5), 1623-1627. doi:10.1017/RDC.2016.117

Reimer P., Austin W., Bard E., Bayliss A., Blackwell P., Bronk Ramsey C., Butzin M., Cheng H., Edwards R.L., Friedrich M., Grootes P.M., Guilderson T.P., Haidas I., Heaton T.J., Hogg A.G., Hughen K.A., Kromer B., Manning S.W., Muscheler R., Palmer J.G., Pearson C., van der Plicht J., Reimer R.W., Richards D.A., Scott E.M., Southon J.R., Turney C.S.M., Wacker L., Adolphi F., Büntgen U., Capano M., Fahrni S.M., Fogtmann-Schulz A., Friedrich R., Köhler P., Kudsk S., Miyake F., Olsen J., Reinig F., Sakamoto M., Sookdeo A., Talamo S. (2020). The IntCal20 Northern Hemisphere Radiocarbon Age Calibration Curve (0–55 cal kBP). Radiocarbon, 62(4), 725-757. doi:10.1017/RDC.2020.41

Riva R.E.M., Gunter B.C., Urban T.J., Vermeersen B.L.A., Lindenbergh R.C., Helsen M.M., Bamber J.L., van de Wal R.S.W., van den Broeke M.R., Schutz B.E. (2009). Glacial Isostatic Adjustment over Antarctica from combined ICESat and GRACE satellite data. Earth and Planetary Science Letters, Vol. 288, Issues 3–4, P. 516-523, ISSN 0012-821X, https://doi.org/10.1016/j.epsl.2009.10.013

Roy K., Peltier W.R. (2015). Glacial isostatic adjustment, relative sea level history and mantle viscosity: reconciling relative sea level model predictions for the U.S. East coast with geological constraints, Geophysical Journal International, vol. 201, Issue 2, p.1156–1181, https://doi.org/10.1093/gji/ggv066

Ruddiman, W. F. (2008). Earth's climate: Past and future. New York: W.H. Freeman.

Sabadini R., Yuen D. A., Gasperini P. (1985). The effects of transient rheology on the interpretation of lower mantle viscosity. Geophysical Research Letters, Vol. 12, Issue 6, 0094-8276 https://doi.org/10.1029/GL012i006p00361

Shennan, I. (1986). Flandrian sea-level changes in the Fenland, II: tendencies of sea level movement, altitudinal changes and local and regional factors. Journal of Quaternary Science vol. 1, p. 155–179, https://doi.org/10.1002/jqs.3390010205

Shennan, I. (2015), Framing research questions, in: Shennan, I., Long, A.J., Horton, B.P. (Eds.), Handbook of Sea-Level Research. John Wiley & Sons, pp. 3–25.

Shipp, R.C., Belknap, D.F., Kelley, J.T. (1991), Seismic-stratigraphic and geomorphic evidence for a post-glacial sea-level lowstand in the northern Gulf of Maine. Journal of Coastal Research 341–364.

Siddiquie H., Bhattacharya G., Pathak M. and Qasim S. (1983). Indira Mount — An Underwater Mountain in the Antarctic Ocean. Scientific report of first Indian Expedition to Antarctica (DOD Tech. Publ.; 1). 161-165.

Simpson M.J.R., Milne G.A., Huybrechts P., Long A.J. (2009) Calibrating a glaciological model of the Greenland ice sheet from the Last Glacial Maximum to present-day using field observations of relative sea level and ice extent. Quaternary Science Reviews, Vol. 28, Issues 17–18, P. 1631-1657, ISSN 0277-3791, https://doi.org/10.1016/j.quascirev.2009.03.004

Slangen A.B.A., Katsman C.A., van de Wal R.S.W. et al. (2012) Towards regional projections of twenty-first century sea-level change based on IPCC SRES scenarios. Clim Dyn 38, 1191–1209. https://doi.org/10.1007/s00382-011-1057-6

Stuiver, M., Borns Jr, H.W. (1975), Late Quaternary marine invasion in Maine: its chronology and associated crustal movement. Geological Society of America Bulletin 86, 99–104.

Stuiver, M., & Polach, H. (1977). Discussion Reporting of 14C Data. Radiocarbon, 19(3), 355-363. doi:10.1017/S0033822200003672

Stuiver, M., Reimer, P.J., and Reimer, R.W. (2022), CALIB 8.2 [WWW program] at http://calib.org

Suchanek, T.H. (1978), The ecology of Mytilus edulis L. in exposed rocky intertidal communities. Journal of Experimental Marine Biology and Ecology 31, 105–120.

Tang H., Chen Y. (2013). Global glaciations and atmospheric change at ca. 2.3 Ga. Geoscience Frontiers, Vol. 4, Issue 5, P. 583-596, ISSN 1674-9871, https://doi.org/10.1016/j.gsf.2013.02.003

Tarasov, L., Dyke, A. S., Neal, R. M., & Peltier, W. R. A. (2012). Data-calibrated distribution of deglacial chronologies for the North American ice complex from glaciological modeling. Earth and Planetary Science Letters, 315-316, 30-40. https://doi.org/10.1016/j.epsl.2011.09.010

Theroux, R.B., Wigley, R.L. (1983), Distribution and abundance of east coast bivalve mollusks based on specimens in the National Marine Fisheries Service Woods Hole Collection. US Department of Commerce, National Oceanic and Atmospheric Administration.

Thompson, W.B., Crossen, K.J., Andersen, B.G. (1989), Glaciomarine Deltas of Maine and Their Relation to Late Pleistocene-Holocene Crustal Movements. Maine Geological Survey, Bulletin 40, 43-67.

Thompson, W.B., Griggs, C.B., Miller, N.G., Nelson, R.E., Weddle, T.K., Kilian, T.M. (2011), Associated terrestrial and marine fossils in the late-glacial Presumpscot Formation, southern Maine, USA, and the marine reservoir effect on radiocarbon ages. Quaternary Research 75, 552–565.

Tyler-Walters, H. (2003), Mya arenaria Sand gaper. In Tyler-Walters H. and Hiscock K. (eds) Marine Life Information Network: Biology and Sensitivity Key Information Reviews, [on-line]. Plymouth: Marine Biological Association of the United Kingdom. Available from: https://www.marlin.ac.uk/species/detail/1404

Tyler-Walters, H. (2007), Modiolus modiolus Horse mussel. In Tyler-Walters H. and Hiscock K. (eds) Marine Life Information Network: Biology and Sensitivity Key Information Reviews, [on-line]. Plymouth: Marine Biological Association of the United Kingdom. Available from: https://www.marlin.ac.uk/species/detail/1532

Tyler-Walters, H. (2008), Mytilus edulis Common mussel. In Tyler-Walters H. and Hiscock K. (eds) Marine Life Information Network: Biology and Sensitivity Key Information Reviews, [on-line]. Plymouth: Marine Biological Association of the United Kingdom. Available from: https://www.marlin.ac.uk/species/detail/1421

Vacchi M., Engelhart S.E., Nikitina D., Ashe E.L., Peltier W. R., Roy K., Kopp R.E., Horton B.P. (2018) Postglacial relative sea-level histories along the eastern Canadian coastline. Quaternary Science Reviews, Volume 201, Pages 124-146, ISSN 0277-3791. https://doi.org/10.1016/j.quascirev.2018.09.043

Van den Berg A.P., van Keken P.E., Yuen D.A. (1993) The effects of a composite non-Newtonian and Newtonian rheology on mantle convection. Geophysical Journal International, Vol. 115, Issue 1, October 1993, P. 62–78, https://doi.org/10.1111/j.1365-246X.1993.tb05588.x

Van de Plassche, O. (1986), Sea-level research: A manual for the collection and evaluation of data: Norwich. UK, Geobooks.

Whitehouse P.L. (2018) Glacial isostatic adjustment modelling: historical perspectives, recent advances, and future directions. Earth Surf. Dynam., Vol. 6, p. 401–429. https://doi.org/10.5194/esurf-6-401-2018

Wu P., Wang H. (2008) Postglacial isostatic adjustment in a self-gravitating spherical earth with power-law rheology. Journal of Geodynamics,Vol. 46, Issues 3–5, p. 118-130, ISSN 0264-3707, https://doi.org/10.1016/j.jog.2008.03.008

Yousefi, M., Milne, G. A., Love, R., and Tarasov, L. (2018) Glacial isostatic adjustment along the Pacific coast of central North America. Quaternary Science Reviews, vol. 193, pp. 288–311. https://doi.org/10.1016/j.quascirev.2018.06.017

Yousefi, M. (2021) Observations of uplift and subsidence along the North American Pacific coast - illuminating the geodynamic complexity of an active margin. https://doi.org/10.5194/egusphere-egu21-12174

Zwarts, L., Wanink, J. (1989), Siphon size and burying depth in deposit-and suspension-feeding benthic bivalves. Marine Biology 100, 227–240.